Updated global fit of the aligned two-Higgs-doublet model with heavy scalars

Anirban Karan,[1,*] Víctor Miralles,[2,†] and Antonio Pich[1,‡]

[1]*Institut de Física Corpuscular (CSIC-UV), Parc Cientifc, Catedrático José Beltrán 2, E-46980 Paterna, Spain*

[2]*INFN, Sezione di Roma, Piazzale A. Moro 2, I-00185 Roma, Italy*

(Received 18 September 2023; accepted 29 December 2023; published 15 February 2024)

An updated global fit on the parameter-space of the aligned two-Higgs-doublet model is performed with the help of the open-source package HEPfit, assuming the Standard-Model Higgs to be the lightest scalar. No new sources of *CP* violation, other than the phase in the Cabibbo-Kobayashi-Maskawa matrix of the Standard Model, are considered. A similar global fit was previously performed by O. Eberhardt *et al.* [Global fits in the aligned two-Higgs-doublet model, J. High Energy Phys. 05 (2021) 005] with a slightly different set of parameters. Our updated fit incorporates improved analyses of the theoretical constraints required for the perturbative unitarity and boundedness of the scalar potential from below, additional flavor observables and updated data on direct searches for heavy scalars at the LHC, Higgs signal strengths, and electroweak precision observables. Although not included in the main fit, the implications of the CDF measurement of the $W^{\pm}$ mass are also discussed.

DOI: 10.1103/PhysRevD.109.035012

I. INTRODUCTION

With the discovery of the Higgs boson [1,2], the Standard Model (SM) has become a well-established theory describing the interactions among elementary particles in a very elegant way. Nonetheless, there is ample evidence indicating that the SM cannot explain all aspects of nature, and hence the existence of physics beyond-the-SM (BSM) is indispensable. In order to explain such BSM phenomena, the SM is usually enlarged with some additional particles or gauge groups that respect all of its fundamental principles. While the augmentation of the SM with extra generations of quarks and leptons receives severe experimental constraints from unitarity-triangle data [3] or Z-boson branching fractions [4], extensions with additional $SU(2)_L$ scalar doublets do not suffer from such stringent bounds.[1]

Among such scalar extensions, the simplest one is the two-Higgs-doublet model (THDM), where one additional scalar doublet with the same quantum numbers as the SM Higgs doublet is appended [6–8]. In addition to the three needed Goldstone bosons, this model includes three neutral and one pair of charged scalars. Such a rich scalar spectrum opens various interesting possibilities such as new sources of *CP* violation [9–13], axion-like phenomenology [14–16], dark matter aspects [17–19], neutrino mass generation [20,21], electroweak baryogenesis [22–24], the stability of the scalar potential until the Planck scale [25–27], etc. Moreover, the THDM can also be thought of as a low-energy effective field theory framework for several models with larger symmetry groups (like supersymmetry).

One major shortcoming of the most general THDM is the emergence of tree-level flavor-changing neutral currents (FCNCs), which are observed to be tightly constrained experimentally. This problem is usually avoided by imposing discrete $\mathcal{Z}_2$ symmetries so that each type of right-handed fermion couples to one scalar doublet only [28,29]. However, the absence of tree-level FCNCs can be guaranteed with a much weaker requirement: the alignment of Yukawa couplings in the flavor space, so that the interactions of the two scalar doublets acquire the same flavor structure [30–33]. This provides a more generic theoretical framework, known as the "aligned THDM" (ATHDM), where flavor violation is minimal [34,35] and (highly suppressed) FCNCs only appear at higher perturbative orders [30–32,36–43]. In this model, all of the fermion-scalar interactions become proportional to

*kanirban@ific.uv.es

†victor.miralles@roma1.infn.it

‡antonio.pich@ific.uv.es

[1]In generic scalar extensions, the tree-level value of the ρ parameter shifts from unity, depending on the hypercharge and weak isospin of the extra scalars [5]. However, it remains equal to 1 with additional doublets having the same hypercharge as the SM Higgs doublet.

the masses of the corresponding fermions, leading to a quite compelling phenomenology in high-energy colliders [43–45] and low-energy flavor experiments [37,46,47]. The ATHDM constitutes a generic platform for THDMs; all $\mathcal{Z}_2$-symmetric THDM scenarios can be explored as special cases of the ATHDM [30]. In addition, the ATHDM can accommodate new sources of CP violation beyond the Cabibbo-Kobayashi-Maskawa (CKM) matrix in both the scalar and Yukawa sectors [30].

The parameter space of the THDM has been extensively scrutinized in the literature, considering LHC data, LEP data, flavor bounds, and theoretical constraints [37,43–45,48–76]. A global fit of the ATHDM with no new sources of CP violation (and a slightly different set of parameters) was performed in Ref. [74], taking into account various theoretical and experimental bounds. In this paper, we reanalyze the global fit of this scenario in great detail, assuming that the SM Higgs boson is the lightest scalar. The fits are performed with the help of the open-source code HEPfit [77]. Compared with the previous study, we update the Higgs signal strengths and add direct searches for all of the scalars from the most recent LHC data. Additionally, we improve the analysis of theoretical constraints by including *necessary and sufficient* conditions for boundedness of the scalar potential from below (i.e., the potential never tends to negative infinity) and incorporate the branching fractions for semileptonic decays of B, D, and K mesons in the flavor sector too. We also analyze the implications of the CDF measurement of the $W^{\pm}$ mass [78], although we do not include it in our global fits in view of its currently unresolved discrepancy with other measurements. A similar conservative attitude has been taken for the muon $g-2$ anomaly [79], in view of the current controversy with lattice [80–82] and τ-decay [83,84] data; although not included in the global fit, we also study the ensuing constraints on the parameter space of the ATHDM.

The paper is organized in the following way. Section II briefly describes the ATHDM scenario. The setup for the global fit is discussed in Sec. III. While in Sec. IV we illustrate different theoretical and experimental constraints that are considered for this study, in the Sec. V we present the numerical results from the fits. Finally, we conclude in Sec. VI. All of the data and various other details used in the global fit are incorporated in the Appendices.

II. THE ATHDM MODEL

A. Scalar sector

We extend the SM with a second complex scalar doublet having the same hypercharge as the SM scalar doublet, i.e., $Y=1/2$. The neutral components of both scalar doublets may acquire nonzero complex vacuum expectation values (VEV); nonetheless, with a suitable $SU(2)_L \otimes U(1)_Y$ global transformation, one can always rotate the basis of the scalar space such that only the neutral component of the first doublet acquires a nonzero (real) VEV. Working in this so-called Higgs basis, we can write down the two doublet scalar fields as

$$\Phi_1 = \frac{1}{\sqrt{2}}\begin{pmatrix} \sqrt{2}G^+ \\ S_1 + v + iG^0 \end{pmatrix}, \qquad \Phi_2 = \frac{1}{\sqrt{2}}\begin{pmatrix} \sqrt{2}H^+ \\ S_2 + iS_3 \end{pmatrix}, \tag{2.1}$$

where Φ_1 gets the VEV $v = 246$ GeV. The components $G^{\pm}$ and G^0 act as Goldstone bosons, providing the masses to the $W^{\pm}$ and Z bosons. Thus, we are left with one pair of charged scalars $H^{\pm}$, two neutral scalars $S_{1,2}$, and one neutral pseudoscalar S_3. The three neutral particles S_j mix with each other through an orthogonal transformation to produce the mass eigenstates φ_i^0. The explicit form of this orthogonal transformation depends on the scalar potential. In general, if the scalar potential is not invariant under the CP symmetry, all three S_j fields mix together, giving no definite CP to the mass eigenstates.

The most general scalar potential, allowed by the SM gauge symmetry, takes the form

$$\begin{aligned} V = {} & \mu_1 \Phi_1^\dagger \Phi_1 + \mu_2 \Phi_2^\dagger \Phi_2 + [\mu_3 \Phi_1^\dagger \Phi_2 + \text{H.c.}] + \frac{\lambda_1}{2}(\Phi_1^\dagger \Phi_1)^2 \\ & + \frac{\lambda_2}{2}(\Phi_2^\dagger \Phi_2)^2 + \lambda_3 (\Phi_1^\dagger \Phi_1)(\Phi_2^\dagger \Phi_2) \\ & + \lambda_4 (\Phi_1^\dagger \Phi_2)(\Phi_2^\dagger \Phi_1) + \left[\left(\frac{\lambda_5}{2}\Phi_1^\dagger \Phi_2 + \lambda_6 \Phi_1^\dagger \Phi_1 \right.\right. \\ & \left.\left. + \lambda_7 \Phi_2^\dagger \Phi_2\right)(\Phi_1^\dagger \Phi_2) + \text{H.c.}\right], \end{aligned} \tag{2.2}$$

where μ_3, λ_5, λ_6, and λ_7 are complex parameters and the rest are real. Minimizing the potential with respect to the neutral fields at their corresponding minima, one obtains

$$v^2 = -\frac{2\mu_1}{\lambda_1} = -\frac{2\mu_3}{\lambda_6}, \tag{2.3}$$

implying that μ_1 and μ_3 are not independent quantities. Redefining the phase of Φ_2, one can make any one of the three parameters λ_5, λ_6, or λ_7 real. Therefore, the scalar potential involves 11 independent real parameters: μ_2, v, $\lambda_{1,2,3,4}$, $|\lambda_{5,6,7}|$, and the two relative phases between $\lambda_{5,6,7}$.

The quadratic terms of the potential, which give rise to the scalar masses, can be written as

$$\begin{aligned} V_M = {} & \left(\mu_2 + \frac{1}{2}\lambda_3 v^2\right) H^+ H^- \\ & + \frac{1}{2}\begin{pmatrix} S_1 & S_2 & S_3 \end{pmatrix} \mathcal{M} \begin{pmatrix} S_1 \\ S_2 \\ S_3 \end{pmatrix}, \end{aligned} \tag{2.4}$$

with

$$\mathcal{M} = \begin{pmatrix} v^2\lambda_1 & v^2\mathrm{Re}(\lambda_6) & -v^2\mathrm{Im}(\lambda_6) \\ v^2\mathrm{Re}(\lambda_6) & \mu_2 + \frac{1}{2}v^2\{\lambda_3+\lambda_4+\mathrm{Re}(\lambda_5)\} & -\frac{1}{2}v^2\mathrm{Im}(\lambda_5) \\ -v^2\mathrm{Im}(\lambda_6) & -\frac{1}{2}v^2\mathrm{Im}(\lambda_5) & \mu_2 + \frac{1}{2}v^2\{\lambda_3+\lambda_4-\mathrm{Re}(\lambda_5)\} \end{pmatrix}. \tag{2.5}$$

In order to obtain the physical mass eigenstates, we need to diagonalize the neutral mass matrix (2.5). Imposing CP conservation in the scalar sector, all of the parameters in our potential become real, reducing the number of independent inputs to nine. Moreover, in this case the mass eigenstates have definite CP: we get two CP-even (h, H) and one CP-odd (A) field. From the mass matrix, we explicitly see that in this case $S_3 = A$ does not mix with the other scalars and we only need to diagonalize a 2×2 matrix. The squared masses are then given by

$$M^2_{H^\pm} = \mu_2 + \frac{\lambda_3}{2}v^2, \qquad M^2_{h,H} = \frac{1}{2}(\Sigma \mp \Delta),$$
$$M^2_A = M^2_{H^\pm} + \frac{v^2}{2}(\lambda_4 - \lambda_5), \tag{2.6}$$

with

$$\Sigma = M^2_{H^\pm} + \left(\lambda_1 + \frac{\lambda_4}{2} + \frac{\lambda_5}{2}\right)v^2 \quad \text{and}$$
$$\Delta = \sqrt{(\Sigma - 2\lambda_1 v^2)^2 + 4\lambda_6^2 v^4}. \tag{2.7}$$

Note also that, since the trace of the mass matrix must be invariant, the scalar masses must satisfy the relation

$$M^2_h + M^2_H + M^2_A = 2M^2_{H^\pm} + v^2(\lambda_1 + \lambda_4), \tag{2.8}$$

which can also be easily confirmed by substituting the expressions for the masses. The mixing between the two CP-even neutral scalars,

$$\begin{pmatrix} h \\ H \end{pmatrix} = \begin{pmatrix} \cos\tilde{\alpha} & \sin\tilde{\alpha} \\ -\sin\tilde{\alpha} & \cos\tilde{\alpha} \end{pmatrix}\begin{pmatrix} S_1 \\ S_2 \end{pmatrix}, \tag{2.9}$$

is given by

$$\tan\tilde{\alpha} = \frac{M^2_h - v^2\lambda_1}{v^2\lambda_6} = \frac{v^2\lambda_6}{v^2\lambda_1 - M^2_H}. \tag{2.10}$$

Using the above equations, we can trade five of the nine parameters of the potential (μ_2, v, and λ_{1-7}) for the four scalar masses ($M_{H^\pm}, M_h, M_H, M_A$) and the mixing angle $\tilde{\alpha}$, which are more physical. Clearly, λ_2 must be kept since it does not relate with any of the new parameters. Since μ_2 and λ_3 always appear in the same combination ($M_{H^\pm}$), we must keep one of them, which we choose to be λ_3. From Eq. (2.10) we can relate λ_1 and λ_6 with $\tilde{\alpha}$, M^2_h, M^2_H, and v. Then, we can use Eq. (2.8) to obtain λ_4 and Σ to obtain λ_5.

With this procedure, we trade μ_2, λ_1, λ_4, λ_5, and λ_6 for the four masses and the mixing angle. Our choice for the nine input parameters is then $v, M_{H^\pm}, M_h, M_H, M_A, \tilde{\alpha}, \lambda_2, \lambda_3$, and λ_7. The remaining parameters of the scalar potential can be easily obtained in terms of these inputs:

$$\mu_2 = M_{H^\pm} - \frac{\lambda_3}{2}v^2, \qquad \lambda_1 = \frac{M^2_h + M^2_H\tan^2\tilde{\alpha}}{v^2(1+\tan^2\tilde{\alpha})},$$
$$\lambda_6 = \frac{(M^2_h - M^2_H)\tan\tilde{\alpha}}{v^2(1+\tan^2\tilde{\alpha})},$$
$$\lambda_4 = \frac{1}{v^2}\left(M^2_h + M^2_A - 2M^2_{H^\pm} + \frac{M^2_H - M^2_h}{1+\tan^2\tilde{\alpha}}\right),$$
$$\lambda_5 = \frac{1}{v^2}\left(\frac{M^2_H + M^2_h\tan^2\tilde{\alpha}}{1+\tan^2\tilde{\alpha}} - M^2_A\right). \tag{2.11}$$

While considering interactions of neutral scalars with gauge bosons, S_1 plays the role of the SM Higgs boson. This implies that the couplings of the scalar mass eigenstates with a pair of gauge bosons are given by

$$g_{hVV} = \cos\tilde{\alpha}\, g^{\mathrm{SM}}_{hVV}, \qquad g_{HVV} = -\sin\tilde{\alpha}\, g^{\mathrm{SM}}_{hVV}, \qquad g_{AVV} = 0, \tag{2.12}$$

where $VV \equiv W^+W^-, ZZ$.

B. Yukawa sector

The interactions of the fermion mass eigenstates with the scalar fields read

$$\begin{aligned} -\mathcal{L}_Y = &\left(1+\frac{S_1}{v}\right)\{\bar{u}_L M_u u_R + \bar{d}_L M_d d_R + \bar{l}_L M_l l_R\} \\ &+ \frac{1}{v}(S_2 + iS_3)\{\bar{u}_L Y_u u_R + \bar{d}_L Y_d d_R + \bar{l}_L Y_l l_R\} \\ &+ \frac{\sqrt{2}}{v}H^+\{\bar{u}_L V Y_d d_R - \bar{u}_R Y_u^\dagger V d_L + \bar{\nu}_L Y_l l_R\} + \mathrm{H.c.}, \end{aligned} \tag{2.13}$$

where the generation indices are suppressed and the subscripts L, R denote the usual left and right chiral fields. Here, $M_f (f \equiv u, d, l)$ are diagonal mass matrices for the up-type quark, down-type quarks, and charged leptons, respectively, originating from the Yukawa interactions with the doublet Φ_1. Y_f are the Yukawa matrices parametrizing the fermionic couplings with the second doublet Φ_2, and V is the usual CKM matrix required for the quark mixing.

In general, Y_f could be arbitrary 3×3 complex matrices, which leads to unwanted FCNCs at tree level. This can be easily avoided by imposing the alignment condition of M_f and Y_f in flavor space [30,31], i.e.,

$$Y_u = \varsigma_u^* M_u \quad \text{and} \quad Y_{d,l} = \varsigma_{d,l} M_{d,l}, \tag{2.14}$$

where the Yukawa alignment parameters ς_f could be arbitrary complex numbers. In terms of the scalar and fermion mass eigenstates, the Yukawa Lagrangian takes then the form

$$-\mathcal{L}_Y = \sum_{i,f} \left(\frac{y_f^{\varphi_i^0}}{v} \right) \varphi_i^0 [\bar{f} M_f \mathcal{P}_R f] + \left(\frac{\sqrt{2}}{v} \right) H^+ \left[\bar{u} \left\{ \varsigma_d V M_d \mathcal{P}_R - \varsigma_u M_u^\dagger V \mathcal{P}_L \right\} d + \varsigma_l \bar{\nu} M_l \mathcal{P}_R l \right] + \text{H.c.}, \tag{2.15}$$

where $\mathcal{P}_{L,R}$ are chirality projection operators and φ_i^0 are the scalar mass eigenstates.

In the following, we assume a CP-conserving potential and that there are no additional sources of CP violation beyond the CKM phase, i.e., we only consider real alignment parameters. The Yukawa couplings of the neutral scalars are then given by

$$y_u^H = -\sin\tilde{\alpha} + \varsigma_u \cos\tilde{\alpha}, \qquad y_u^h = \cos\tilde{\alpha} + \varsigma_u \sin\tilde{\alpha}, \qquad y_u^A = -i\varsigma_u, \tag{2.16}$$

$$y_{d,l}^H = -\sin\tilde{\alpha} + \varsigma_{d,l} \cos\tilde{\alpha}, \qquad y_{d,l}^h = \cos\tilde{\alpha} + \varsigma_{d,l} \sin\tilde{\alpha}, \qquad y_{d,l}^A = i\varsigma_{d,l}. \tag{2.17}$$

The usual THDM scenarios based on $\mathcal{Z}_2$ symmetries are just particular cases of the more general ATHDM framework; they can be retrieved by imposing $\mu_3 = \lambda_6 = \lambda_7 = 0$ along with the following conditions:

$$\begin{aligned} &\text{Type I:}\ \varsigma_u = \varsigma_d = \varsigma_l = \cot\beta, \qquad \text{Type II:}\ \varsigma_u = -\frac{1}{\varsigma_d} = -\frac{1}{\varsigma_l} = \cot\beta, \qquad \text{Inert:}\ \varsigma_u = \varsigma_d = \varsigma_l = 0, \\ &\text{Type X:}\ \varsigma_u = \varsigma_d = -\frac{1}{\varsigma_l} = \cot\beta \quad \text{and} \quad \text{Type Y:}\ \varsigma_u = -\frac{1}{\varsigma_d} = \varsigma_l = \cot\beta. \end{aligned} \tag{2.18}$$

The alignment requirement (2.14) remains stable under renormalization when it is protected by $\mathcal{Z}_2$ symmetries [36]. Otherwise, higher-order quantum corrections create a misalignment of M_f and Y_f that generates loop-suppressed FCNC effects. However, the special Yukawa structure of the ATHDM strongly constrains the possible FCNC interactions, making those effects numerically small [30,31,37]. Assuming exact alignment at some high-energy scale (even at the Planck mass), the small misalignment generated by running down to low energies remains well below the current experimental limits [32,38,39,42].

III. FIT SETUP

Our numerical analyses are performed with the open-source HEPfit package [77]. This code has been widely used due to its efficiency and versatility, allowing for global fits both within the SM [85] or in general BSM extensions such as the SM effective field theory [86,87] or particular models of new physics (NP) [74,88], as in this paper. HEPfit works within the Bayesian statistics framework and therefore we need to carefully choose the priors of our variables. We have a total of ten new degrees of freedom with respect to the SM: the physical masses of the additional scalars ($M_{H^\pm}, M_H$, and M_A), the mixing angle of the CP-even neutral scalars ($\tilde{\alpha}$), three quartic couplings of the potential (λ_2, λ_3, and λ_7), and the three Yukawa alignment parameters (ς_u, ς_d, and ς_l). Since our fits include all of the available information, we use uniform distributions as priors. In general, the priors are chosen to cover the region of the parameters that is physically relevant. For the mixing angle, we chose the prior in such a way that at least the 5σ region of the posterior probability is contained within the selected range. The quartic couplings are mainly constrained from theory assumptions, which impose a hard cut on the values that these parameters can take. In this case, we chose a prior wide enough to include all points allowed by the theory constraints. The priors of the Yukawa couplings are also set within the limits allowed by perturbative constraints.

There is huge freedom when choosing ranges for the scalar masses. In this analysis, we assume that the SM Higgs is the lightest scalar, i.e., that M_H, M_A, and $M_{H^\pm}$ are larger than 125 GeV. The complementary scenario where the SM Higgs is not the lightest scalar is phenomenologically very intriguing and capable of displaying very distinct collider signatures at the LHC [57–59]. However, these signatures and the overall phenomenology are strongly dependent on the assumed hierarchy of scalar masses (which BSM particles are considered to be lighter than

TABLE I. Priors chosen for the NP parameters.

Priors			
$M_{H^\pm} \subset [0.125,\ 1.0\,(1.5)]$ TeV	$M_H \subset [0.125, 1.0\,(1.5)]$ TeV	$M_A \subset [0.125, 1.0\,(1.5)]$ TeV	
$\lambda_2 \subset [0, 11]$	$\lambda_3 \subset [-3, 17]$	$\lambda_7 \subset [-5, 5]$	
$\tilde{\alpha} \subset [-0.16, 0.16]$	$\varsigma_u \subset [-1.5, 1.5]$	$\varsigma_d \subset [-50, 50]$	$\varsigma_l \subset [-100, 100]$

the SM Higgs). Moreover, a detailed analysis of the different possible scenarios requires the inclusion of additional experimental data from LEP and flavor factories and a proper theoretical treatment of hadronic resonances in the mass region below 10 GeV. These intricacies for the light BSM particles are beyond the scope of this paper, and therefore here we focus only on the heavy BSM scenario.[2]

Higher scalar masses are obviously preferred by the data because no clear deviations from the SM have been observed so far. Taking into account that many direct searches have been studying mass ranges up to 1 TeV, this number seems a reasonable higher cutoff for our global analysis. However, we also provide some results in which the highest value of the scalar masses have been set to 1.5 TeV, so that we can get a feeling of how much our results depend on the priors. Finally, we would also like to comment that, instead of taking the masses as fundamental parameters, using the masses squared could also be a well-justified choice. However, as can be seen in Ref. [74], when using a uniform distribution for the masses squared the results depend much more on the ranges of masses analyzed. Therefore, we impose our priors linearly on the scalar mass parameters. The chosen priors can be found in Table I.

IV. FIT CONSTRAINTS

We aim to use as much information as we can in order to constrain the parameter space of the ATHDM. In this work we combine the whole set of theoretical constraints with all relevant experimental limits coming from LHC direct searches, Higgs data, electroweak precision data, and flavor observables.

A. Theoretical considerations

Regarding theoretical constraints, the two conditions that are usually demanded are a scalar potential bounded from below and perturbative unitarity of the S matrix. The requirement that the scalar potential is bounded from below indicates that it should not go to large negative values, which would make it unstable, for any configuration of the fields. For this purpose, it is useful to recast the scalar potential V in the following Minkowskian form [89]:

$$V = -\mathtt{M}_\mu \mathtt{r}^\mu + \frac{1}{2}\Lambda^\mu{}_\nu \mathtt{r}_\mu \mathtt{r}^\nu, \tag{4.1}$$

with

$$\begin{aligned}\mathtt{M}_\mu &= \left(-\frac{\mu_1+\mu_2}{2}, -\mathrm{Re}\,\mu_3, \mathrm{Im}\,\mu_3, -\frac{\mu_1-\mu_2}{2}\right),\\ \mathtt{r}^\mu &= \big(|\Phi_1|^2 + |\Phi_2|^2, 2\mathrm{Re}(\Phi_1^\dagger\Phi_2), 2\mathrm{Im}(\Phi_1^\dagger\Phi_2), |\Phi_1|^2 \\ &\quad - |\Phi_2|^2\big),\end{aligned} \tag{4.2}$$

and

$$\Lambda^\mu{}_\nu = \frac{1}{2}\begin{pmatrix} \frac{1}{2}(\lambda_1+\lambda_2)+\lambda_3 & \mathrm{Re}(\lambda_6+\lambda_7) & -\mathrm{Im}(\lambda_6+\lambda_7) & \frac{1}{2}(\lambda_1-\lambda_2) \\ -\mathrm{Re}(\lambda_6+\lambda_7) & -\lambda_4-\mathrm{Re}\lambda_5 & \mathrm{Im}\lambda_5 & -\mathrm{Re}(\lambda_6-\lambda_7) \\ \mathrm{Im}(\lambda_6+\lambda_7) & \mathrm{Im}\lambda_5 & -\lambda_4+\mathrm{Re}\lambda_5 & \mathrm{Im}(\lambda_6-\lambda_7) \\ -\frac{1}{2}(\lambda_1-\lambda_2) & -\mathrm{Re}(\lambda_6-\lambda_7) & \mathrm{Im}(\lambda_6-\lambda_7) & -\frac{1}{2}(\lambda_1+\lambda_2)+\lambda_3 \end{pmatrix}. \tag{4.3}$$

Diagonalization of the mixed-symmetric matrix[3] $\Lambda^\mu{}_\nu$ produces one "timelike" (Λ_0) and three "spacelike" ($\Lambda_{1,2,3}$) eigenvalues.[4] The scalar potential remains bounded from below when the following two conditions are satisfied [89,90]:

(1) All the eigenvalues are real.
(2) $\Lambda_0 > 0$ with $\Lambda_0 > \Lambda_i\ \forall\ i \in \{1,2,3\}$.

Several *necessary* conditions for the scalar potential to be bounded from below have been listed in Ref. [91]. However, those necessary conditions are comprehended in the two above-mentioned *necessary and sufficient* conditions.

One additional constraint could be imposed on the quartic couplings by demanding that the vacuum of the

[2]In a forthcoming publication we will soon address the possibility of lighter scalars.

[3]Actually, $\Lambda_{\mu\nu}$ is a symmetric matrix and can be diagonalized by a $SO(1,3)$ transformation.

[4]The attributes "timelike" and "spacelike" are related to the corresponding eigenvectors.

scalar potential is a stable neutral minimum.[5] For this purpose, one defines the discriminant of the matrix $\xi\mathbb{I}_4 - \Lambda^\mu{}_\nu$ as

$$D = -\prod_{k=0}^{3}(\xi - \Lambda_k) \quad \text{with} \quad \xi = \frac{M_{H^\pm}^2}{v^2}, \tag{4.4}$$

where the Lagrange multiplier ξ is determined by minimizing the scalar potential V with the constraint[6] $\mathtt{r}^\mu \mathtt{r}_\mu = 0$. The condition for a global minimum is found to be [90] $D > 0$, or $D < 0$ with $\xi > \Lambda_0$. We include this condition in our analysis, requiring a stable neutral minimum. However, removing this constraint does not significantly change our results.

The unitarity of the S matrix ensures that, in order to conserve the total probability, scattering amplitudes do not grow monotonically with energy. Since unitarity emerges from the basic formulation of quantum field theory, it is bound to hold in a complete renormalizable theory while dealing with the full S matrix. However, the unitarity bound does not need to be satisfied by the perturbative calculation of the S matrix to any particular order. The stronger requirement of *perturbative unitarity* enforces the unitarity of the S matrix to be obeyed at every order of perturbation theory. It indirectly indicates that the couplings, in terms of which the perturbative expansion is performed, are not very large and one can safely neglect higher-order contributions. Therefore, imposing perturbative unitarity on all of the $2 \to 2$ scattering amplitudes involving the scalars (both the massive ones and the Goldstone bosons, which account for the $W_L^\pm$ and Z_L) will restrict the quartic couplings λ_i, ensuring that the perturbative expansion of the S matrix does not diverge at high energies. *Tree-level unitarity* is enforced on the $2 \to 2$ scattering matrix of scalars by demanding that

$$(a_j^0)^2 \leq \frac{1}{4} \quad \text{with} \quad (\mathbf{a_0})_{i,f} = \frac{1}{16\pi s}\int_{-s}^{0} dt\, \mathcal{M}_{i\to f}(s,t), \tag{4.5}$$

where $\mathbf{a_0}$ is the matrix of tree-level partial-wave amplitudes and a_j^0 are the corresponding eigenvalues in the jth partial wave. Nevertheless, while considering the scattering of scalars at very high energy, only the S-wave amplitude with $j = 0$ becomes most significant at tree level. Constructing two-scalar scattering states with definite hypercharge and weak isospin (Y, I) and grouping the ones with the same set of quantum numbers, the 25-dimensional[7] matrix $\mathbf{a_0}$ can be expressed in a block-diagonal form:

$$\mathbf{a_0^{++}} = \frac{1}{16\pi} X_{(1,1)}, \qquad \mathbf{a_0^{+}} = \frac{1}{16\pi}\mathrm{diag}[X_{(0,1)}, X_{(1,0)}, X_{(1,1)}],$$
$$\mathbf{a_0^{0}} = \frac{1}{16\pi}\mathrm{diag}[X_{(0,0)}, X_{(0,1)}, X_{(1,1)}, X_{(1,1)}], \tag{4.6}$$

where the superscript indicates the total charge of the initial or final states. Thus, the scattering matrix $\mathbf{a_0}$ is comprised of the following four submatrices [91,94]:

$$X_{(1,0)} = \lambda_3 - \lambda_4, \qquad X_{(1,1)} = \begin{pmatrix} \lambda_1 & \lambda_5 & \sqrt{2}\lambda_6 \\ \lambda_5^* & \lambda_2 & \sqrt{2}\lambda_7^* \\ \sqrt{2}\lambda_6^* & \sqrt{2}\lambda_7^* & \lambda_3 + \lambda_4 \end{pmatrix}, \qquad X_{(0,1)} = \begin{pmatrix} \lambda_1 & \lambda_4 & \lambda_6 & \lambda_6^* \\ \lambda_4 & \lambda_2 & \lambda_7 & \lambda_7^* \\ \lambda_6^* & \lambda_7^* & \lambda_3 & \lambda_5^* \\ \lambda_6 & \lambda_7 & \lambda_5 & \lambda_3 \end{pmatrix},$$
$$X_{(0,0)} = \begin{pmatrix} 3\lambda_1 & 2\lambda_3 + \lambda_4 & 3\lambda_6 & 3\lambda_6^* \\ 2\lambda_3 + \lambda_4 & 3\lambda_2 & 3\lambda_7 & 3\lambda_7^* \\ 3\lambda_6^* & 3\lambda_7^* & \lambda_3 + 2\lambda_4 & 3\lambda_5^* \\ 3\lambda_6 & 3\lambda_7 & 3\lambda_5 & \lambda_3 + 2\lambda_4 \end{pmatrix}. \tag{4.7}$$

The perturbative-unitarity condition (4.5) can be traded in terms of the eigenvalues (e_i) for the above four submatrices by demanding that

$$|e_i| < 8\pi. \tag{4.8}$$

On the other hand, considering the coupling of fermions to the charged scalars, we vary the value of ς_f in the perturbative range satisfying $\sqrt{2}|\varsigma_f| m_f/v < 1$. A more detailed study on the perturbativity of the alignment parameters could be performed based on the procedure mentioned in Ref. [95], which would extend the range of ς_f a bit more. However, for our analysis it is sufficient to consider the above inequality.

[5]This requirement is a bit more restrictive. It can be relaxed by allowing a metastable vacuum with a transition time to the true vacuum larger than the age of the Universe.

[6]The condition $\mathtt{r}^\mu \mathtt{r}_\mu = 0$ ensures that the vacuum is a charge-neutral minimum. It has been proven that neutral and charge-breaking vacua cannot coexist in any THDM [92,93].

[7]For any THDM, there are 14 neutral, eight single-charged, and three doubly charged two-body scalar scattering states possible.

B. Direct searches

Many searches for additional scalars have been developed at the LHC. In order to use those results, we compare the theoretical prediction of the cross section times branching ratio, $\sigma \cdot \mathcal{B}$, for several processes with the exclusion limits obtained by the CMS and ATLAS experimental collaborations.

The experimental data are provided in the form of tables, which compile the values of the 95% upper limits on $\sigma \cdot \mathcal{B}$, as a function of the resonance mass. In these tables, HEPfit performs a linear interpolation if needed. In order to compare the theoretical results with the experimental data, we define the ratio of the theoretical prediction over the experimental upper limit. To this ratio we assign a Gaussian distribution (restricted to positive values) centered at 0 such that the value 1 is excluded with a 95% probability.

All of the channels included in our fit can be found in Appendix A. In Table IV we show the channels included for the charged scalars, while those of the neutral scalars are shown in Tables V–VII. Specifically, in Table V we show the decays into neutral scalars (including the SM Higgs boson); in Table VI the decays into fermions, $\gamma\gamma$, and $Z\gamma$; and in Table VII the decays into weak gauge bosons. When the limits on $\sigma \cdot \mathcal{B}$ provided in the experimental papers also consider a subsequent decay of the SM particles, we show this final decay with parentheses. When the limits on $\sigma \cdot \mathcal{B}$ are provided directly on the decay width of the NP particles to SM particles, but using particular decays of the produced SM particles, we show such SM decays with square brackets.

C. Higgs data

The presence of additional scalars generates relevant effects on the production and decay of the SM Higgs. The one-loop $h \to 2\gamma$ amplitude receives additional contributions from the charged scalar. Furthermore, due to the mixing among the CP-even scalars, the coupling of the SM Higgs with the weak bosons is modified as shown in Eq. (2.12), which changes the Higgs production through vector-boson fusion (VBF) and the associated production with vector bosons (Vh). The decays of the Higgs boson to fermions are also sensitive to the scalar mixing, as shown in Eqs. (2.16) and (2.17), which also modifies the Higgs production through gluon fusion (ggF) and its associated production with $t\bar{t}$ pairs (tth).

The production and subsequent decay of the SM Higgs boson have been measured (or bounds have been set) at the LHC for the most relevant production modes (ggF, VBF, Vh, and tth) and decay channels ($c\bar{c}$, $b\bar{b}$, $\gamma\gamma$, $\mu^+\mu^-$, $\tau^+\tau^-$, WW, $Z\gamma$, and ZZ). These data are parametrized in terms of the Higgs signal strengths, which are defined as the measured cross section times branching ratio for a given production and decay Higgs channel, in units of the SM prediction. Table III in Appendix A compiles the experimental papers from which we take the values of the different Higgs signal strengths relevant to our analysis.

D. Electroweak precision observables

The presence of additional scalars generates contributions to the oblique parameters (also known as Peskin-Takeuchi parameters [96,97]) S, T, and U [98]. The experimental values of these parameters are obtained from global fits of electroweak precision data, using observables directly measured (mainly) at LEP and SLC. Among these observables, we highlight the ratio $R_b \equiv \Gamma(Z \to b\bar{b})/\Gamma(Z \to \text{hadrons})$ [99,100], which is also affected by the additional scalars. Using the values of the oblique parameters from the Particle Data Group (PDG) would be inconsistent in our study because those values do not take into account the NP contamination of R_b. Moreover, since we include R_b directly in our global fit of the ATHDM, the information from this observable cannot be employed to determine the oblique parameters.

In order to obtain noncontaminated values for the oblique parameters, we repeat the electroweak fit by removing R_b from the list of fitted measurements, obtaining the values of S, T, and U that are included as inputs to our analysis. These values are summarized in Table IX of Appendix B 2.

The values of the oblique parameters are also highly dependent on the value of the W-boson mass (M_W). For our baseline results on these parameters, we use the value of M_W quoted by the PDG 2022 [101]. However, in April of 2022 the CDF Collaboration announced a controversial new measurement of M_W [78], which is incompatible with the SM prediction by 7σ. Since there is not yet consensus in the community, we do not include this measurement in our main global fit but instead show how much the results change with the values for the oblique parameters obtained when incorporating this new measurement in a global electroweak fit performed with HEPfit [102,103].[8]

Finally, we also notice that using the three oblique parameters S, T, and U and fitting only S and T (assuming U to be negligible) give very similar results. Therefore, we use only S and T, since it is well known that the THDM contributions to U are highly suppressed [98].

E. Flavor observables

The parameter space of the ATHDM can also be constrained from flavor observables, since the new scalars generate relevant contributions to many of them. However, in order to be able to determine these contributions, we first need to know the numerical values of the CKM parameters. For this work we adopt the Wolfenstein

[8]Note that in these references R_b was also included as an input, but we have checked that repeating the fit of Ref. [103] without R_b leads to very similar results. Therefore, we decide to use the values quoted in the original paper.

parametrization [104], so we need to provide the corresponding values as inputs in our analysis. The world averages quoted in the PDG 2022 [101] originate from SM fits from the CKMFitter [105] and UTfit [3,106] collaborations, which make use of several flavor transitions that could be affected by the additional scalars. The UTfit Collaboration also provides the values of the Wolfenstein parameters when removing the loop processes from the fit [107], which gives the correct values for models in which the tree-level effects of NP are negligible. Nevertheless, for some (small) regions of the parameter space in the ATHDM there could still be some contamination of some of the tree-level processes used to determine the Wolfenstein parameters. For this reason, we repeat this CKM fit using only processes that are not contaminated by the additional scalars. Details on this fit, as well as the resulting numerical values for the CKM parameters, can be found in Appendix B 1. Note also that we use as observables for our ATHDM global fit some processes that are usually taken into account in the CKM fit, like the pseudoscalar-meson leptonic decays, so it is clear that we should remove these processes from our CKM determination.

We consider all relevant flavor observables that constrain the CP-conserving ATHDM, including the contributions to loop processes like the neutral-meson mixing of B_s (ΔM_{B_s}) [37,108], the weak radiative decay $B \to X_s\gamma$ [37,46,47,109–115], and the rare weak leptonic decay $B_s \to \mu^+\mu^-$ [40,116]. Besides these loop processes, we also include some relevant tree-level transitions like the leptonic decays of heavy pseudoscalar mesons ($B \to \tau\nu$, $D_{(s)} \to \mu\nu$ and $D_{(s)} \to \tau\nu$), as well as the ratios of the leptonic decays of light pseudoscalar mesons $[\Gamma(K \to \mu\nu)/\Gamma(\pi \to \mu\nu)]$ and the similar tau decays $[\Gamma(\tau \to K\nu)/\Gamma(\tau \to \pi\nu)]$ [37].

We do not include in our main fit the anomalous magnetic moment of the muon, $(g-2)_\mu$ [117], because there is no full consensus in the community on the SM prediction of this observable. The most recent lattice computations of the hadronic vacuum polarization [80–82] and the estimates from τ decay [83,84] seem to find an SM result much closer to the experimental value [118,119] than the dispersive e^+e^- prediction [79], and additional hints of a possible dispersive underestimate are suggested by a recent QCD analysis of the Adler function [120] and the CMD3 data [121]. Nevertheless, this observable is included in our code and we show the individual constraints obtained with it, comparing these results with the ones obtained using all of the other flavor observables that we have mentioned here.

V. FIT RESULTS

Here we provide the results for all of the fits we perform in this analysis. We first discuss in several subsections the limits obtained using only some subsets of observables, in order to show the relevance that each observable has in the global fit. Afterward, we present the global fit, which provides the main results of this work. We also show how the results of our global fit would change if the new CDF measurement of M_W [78] is included.

A. Theoretical bounds

The theoretical considerations generate constraints on the parameters of the scalar potential. As shown in Sec. II, we have a total of nine degrees of freedom in the CP-conserving potential. The scalar vacuum expectation value and M_h are fixed by the measurement of the Fermi constant in muon decay [101] and the Higgs mass measurement at the LHC [101]. We then have a total of seven degrees of freedom that could be possibly constrained with the theory assumptions. As mentioned before, we trade some of these scalar potential parameters for more physical inputs. Our chosen parameters are the masses of the new scalars, the mixing angle among the CP-even scalars, and the three quartic couplings λ_2, λ_3, and λ_7.

The theoretical constraints on the parameters of the potential can be translated into limits on the scalar mass splittings. Figure 1 displays the resulting constraints on the correlation among the different masses and the correlation of the charged scalar mass with the mixing angle. Note that in this case we show the 100% probability region, since all

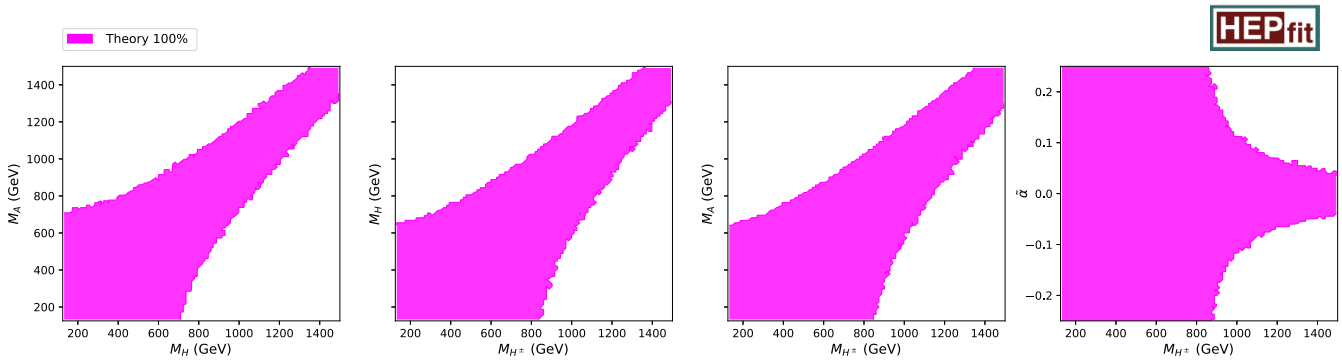

FIG. 1. Constraints from theory assumptions.

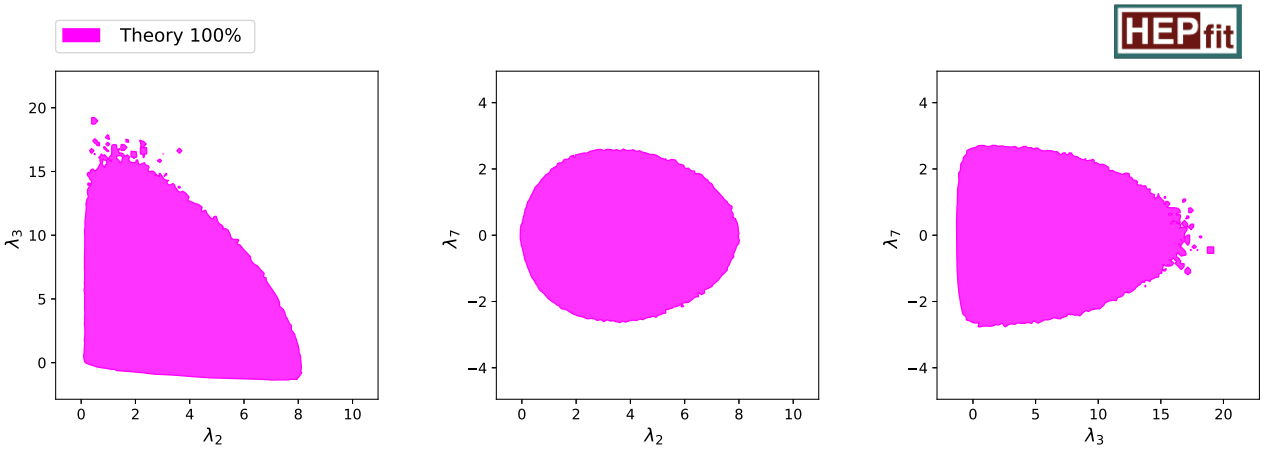

FIG. 2. Constraints from theory assumptions.

of the points that satisfy these constraints are equally valid. In general, we observe that for scalar mass values below 700 GeV, the constraints on the mass splittings and the mixing angle are rather weak. This can be easily understood, since for low masses the mass differences cannot be large enough to reach the theoretical bounds. However, above this threshold, especially beyond 1 TeV, the constraints become considerably more stringent. Since differences of masses squared are proportional to combinations of quartic couplings times the VEV squared, the naive estimate $\sqrt{4\pi}v \approx 870$ GeV gives indeed a good idea of the scale where these limits become relevant.

The constraints on the quartic couplings are shown in Fig. 2, where we can see that negative values of λ_2 are forbidden while slightly negative values of λ_3 could be allowed, provided they are very close to zero. Finally, λ_7 is clearly constrained to be smaller than 3 in modulus.

B. Experimental bounds

Figure 3 shows that the measured Higgs signal strengths generate tight constraints in the $\tilde{\alpha}$-ς_f planes. At 99.7% probability some allowed regions, at the corners of the central and right plots of Fig. 3, appear really far away from the SM solution. These regions correspond to down-type and/or lepton Yukawas of opposite sign to the SM Higgs couplings. Since these observables are only sensitive to the modulus of the Yukawa couplings, this could be a possible solution, although following a Bayesian approach the prior probability of this kind of solutions would be quite small. No such regions appear for up-type quarks because the relative sign between the top Yukawa and the Higgs coupling to the gauge bosons gets constrained by the $h \to 2\gamma$ decay width and the range of allowed $|\varsigma_u|$ values is much smaller.

The oblique parameters (S and T) generate significant constraints on the mass splitting of the additional scalars. These constraints can be found in Fig. 4, where we compare the results obtained when S and T are fitted with the PDG 2022 value of M_W (PDG-M_W) with those using the modified S and T values emerging from the world average [103] after including the CDF M_W (CDF-M_W) measurement [78]. The allowed regions using the PDG

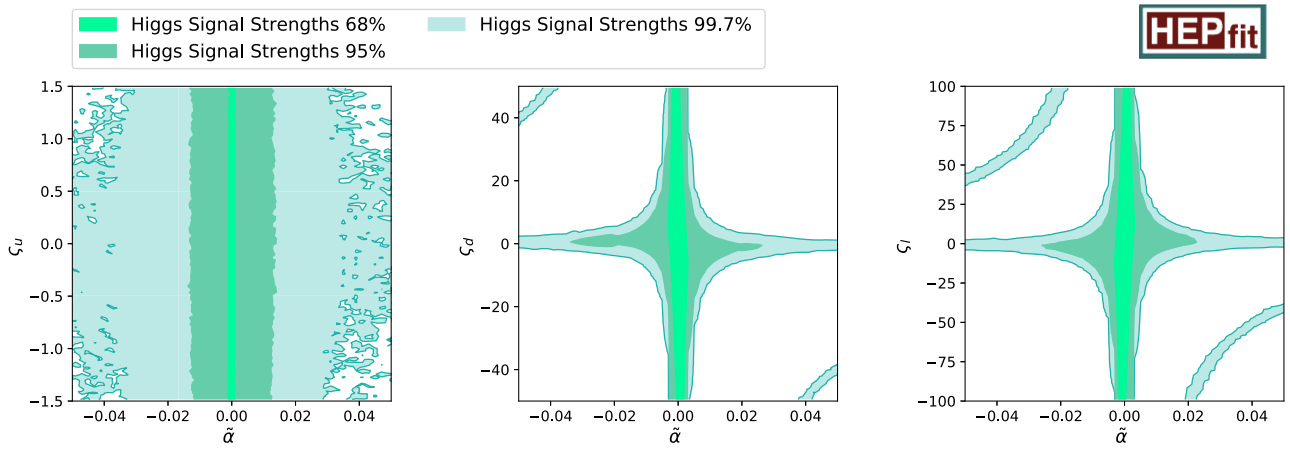

FIG. 3. Constraints from the measured Higgs signal strengths.

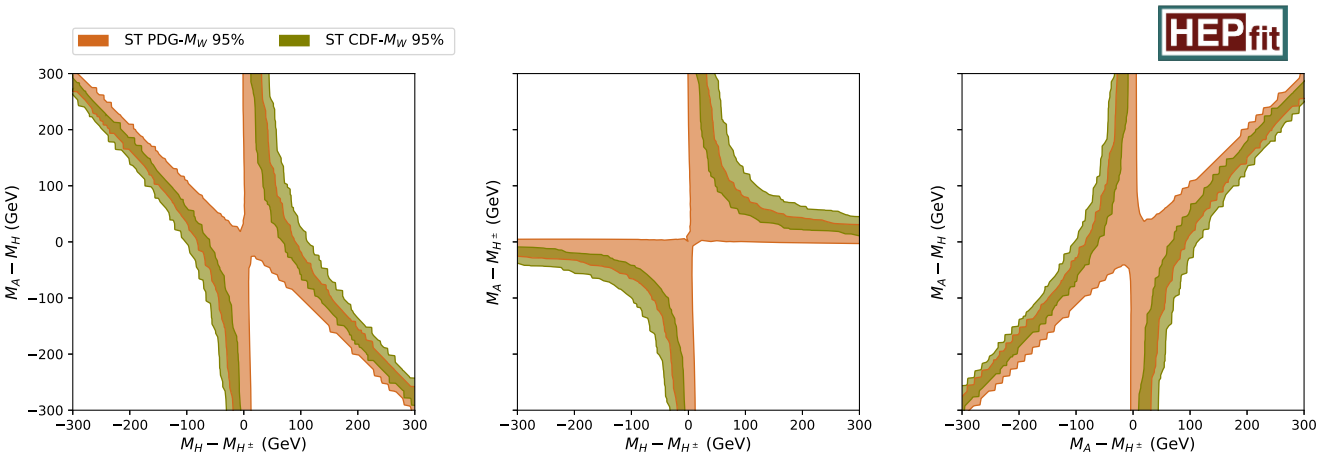

FIG. 4. Constraints on the mass splittings from the oblique parameters S and T.

value of M_W are compatible with small or even zero mass splittings. However, once the CDF value is included in the fit, a nonzero mass difference between the new scalars is definitely required to explain the deviation from the SM prediction of M_W. This scalar mass difference could be accommodated within this model, since we are able to generate the needed contribution to M_W, even when we impose agreement with all other observables in combination, as we discuss in Sec. V D.

The flavor observables and R_b generate constraints on the Yukawa alignment parameters (ς_u, ς_d, ς_l) and the mass of the charged Higgs $M_{H^\pm}$. Figure 5 displays the correlations among ς_u, ς_d, and ς_l, while in Fig. 6 we show the correlation of these parameters with $M_{H^\pm}$. The dominant NP contribution to the $B \to X_s\gamma$ amplitude is proportional to the product $\varsigma_u\varsigma_d$, which explains the strong correlation between these two alignment parameters observed in the left panel of Fig. 5. The first two panels in Fig. 6 also exhibit the presence of two additional bands emerging from the central $B \to X_s\gamma$ allowed region; they correspond to solutions with a NP contribution equal to -2 times the SM amplitude. The strongest constraint on the $\varsigma_u - M_{H^\pm}$ plane comes from meson mixing, although R_b, $B \to X_s\gamma$, and $B_s \to \mu^+\mu^-$ also help in constraining this plane. In the $\varsigma_d - M_{H^\pm}$ plane, the tree-level leptonic and semileptonic decays of pseudoscalar mesons (and tau decays into pseudoscalars) generate the strongest limits for low values of the scalar masses. However, the tree-level NP contributions rapidly drop when increasing the mass of the charged scalar, so for larger mass values the loop processes dominate. $B \to X_s\gamma$ provides the strongest limits for intermediate values of $M_{H^\pm}$ around 500 GeV, while for heavier masses $B_s \to \mu^+\mu^-$ produces the most relevant constraints because it also gets contributions from neutral scalar exchanges that are sizable at large $|\varsigma_d|$. In the $\varsigma_l - M_{H^\pm}$ plane, the constraints are very poor, except at very low values of $M_{H^\pm}$ where useful limits are obtained from the tree-level processes. As shown in the first two panels of Fig. 6, small values of $M_{H^\pm}$ are allowed when $\varsigma_{u,d} \to 0$, but when marginalizing over these two alignment parameters their probability becomes very small, which explains the lower bound on the charged scalar mass observed in the third panel. Notice that the maximum and

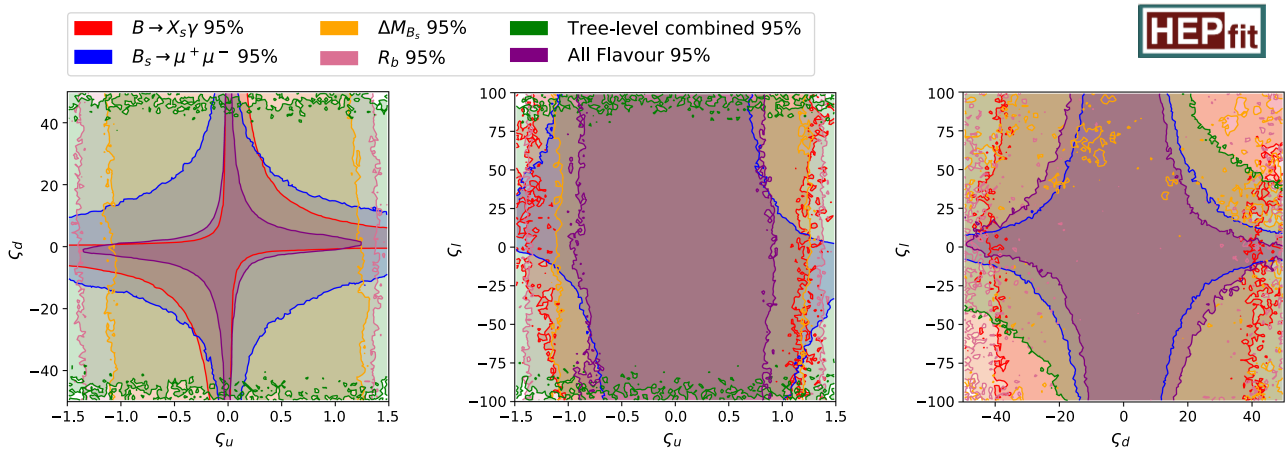

FIG. 5. Constraints from flavor observables on the alignment parameters.

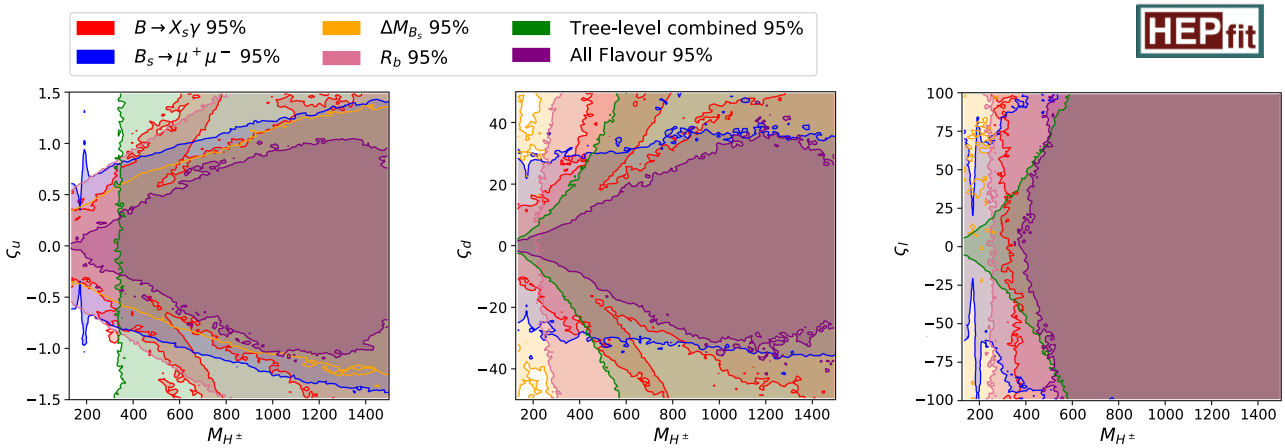

FIG. 6. Constraints from flavor observables on the Yukawa couplings and mass of the charged scalar.

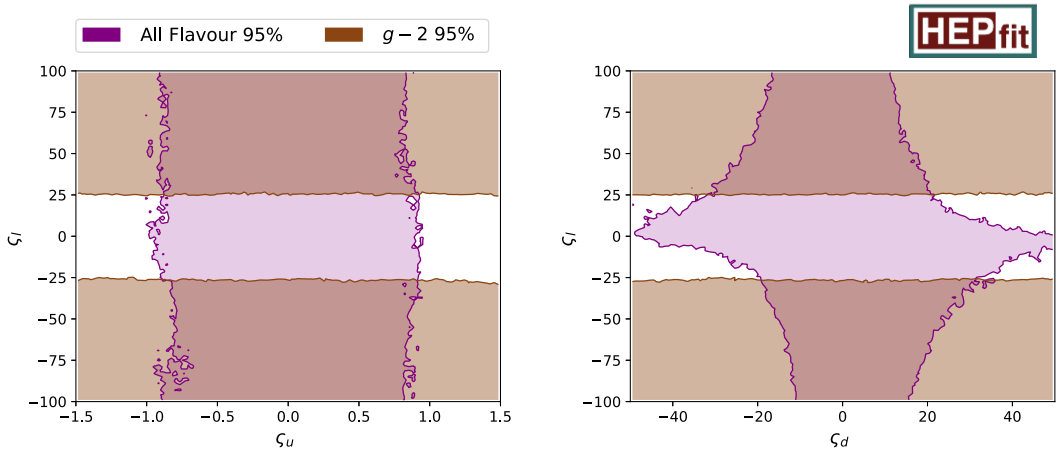

FIG. 7. Comparison of the ς_l region required to accommodate $(g-2)_\mu$ with the flavor constraints.

minimum values allowed for the different parameters are slightly different in Figs. 5 and 6; this is just a consequence of having non-Gaussian distributions.

Finally, in Fig. 7 we compare the constraints on ς_l obtained from the combination of all flavor observables with the results needed to explain the anomalous magnetic moment of the muon. Since we are only considering scalar masses above 125 GeV, quite large values of the leptonic alignment parameter are required, but there is indeed room to satisfy all of the flavor constraints in combination with $(g-2)_\mu$. Nevertheless, we decide to exclude this observable from our global fit because its SM prediction is currently under debate, as discussed in Sec. IV E.

C. Global fits

In this section we provide the results emerging from the global fit, using all of the experimental observables and theoretical considerations at the same time. As mentioned in Sec. III, we consider masses up to 1 and 1.5 TeV, in such a way that we can also explicitly see the dependence on the adopted priors. The marginalized probabilities, given in Table II, indeed exhibit some dependence on the priors, especially regarding the mass limits. This behavior is reasonable since the likelihood is maximized for higher values of the masses; smaller masses would always be disfavored, moving the 95% region farther away when we allow for higher mass values. The allowed ranges of the Yukawa alignment parameters are also wider when heavier masses are allowed because the scalar contributions to the flavor observables decrease with increasing mass values and, therefore, higher values of $\varsigma_{u,d,l}$ become possible, as can be observed in Fig. 6. In contrast, the preferred region of the mixing angle shrinks when we scan over heavier masses because the theoretical constraints, shown in Fig. 1, become more severe for higher values of the scalar masses.

The correlations among the scalar masses are shown in Fig. 8, which exhibits diagonal bands enforced by the theoretical constraints and the oblique parameters. The bounds on the masses get significantly relaxed, and almost

TABLE II. Marginalized individual results. The mass limits are at 95% probability, while for the others we show the mean value and the square root of the variance.

Marginalized individual results			
Masses up to 1 TeV			
$M_{H^\pm} \geq 390$ GeV	$M_H \geq 410$ GeV	$M_A \geq 370$ GeV	
λ_2: 3.2 ± 1.9	λ_3: 5.9 ± 3.5	λ_7: 0.0 ± 1.1	
$\tilde{\alpha}$: $(0.05 \pm 21.0) \times 10^{-3}$	ς_u: 0.006 ± 0.257	ς_d: 0.12 ± 4.12	ς_l: -0.39 ± 11.69
Masses up to 1.5 TeV			
$M_{H^\pm} \geq 480$ GeV	$M_H \geq 490$ GeV	$M_A \geq 480$ GeV	
λ_2: 3.2 ± 1.9	λ_3: 5.9 ± 3.8	λ_7: 0.0 ± 1.2	
$\tilde{\alpha}$: $(0.8 \pm 16.8) \times 10^{-3}$	ς_u: -0.011 ± 0.407	ς_d: -0.096 ± 6.22	ς_l: -1.18 ± 17.54

disappear, in the limit of zero mass splittings between the charged and neutral scalars. This is due to the reduction of the constraints from the oblique parameters, which makes these points much more favored. The correlations among the mass splittings are shown in Fig. 9. In the middle plot one observes that the two mass differences between the charged scalar and the neutral CP-even and CP-odd bosons cannot be simultaneously large; when one increases, the other must decrease. From the left and right plots we can also see that when the mass splitting among the neutral scalars gets large the mass splitting among the charged scalar and one of the neutral scalars must go to zero. Here

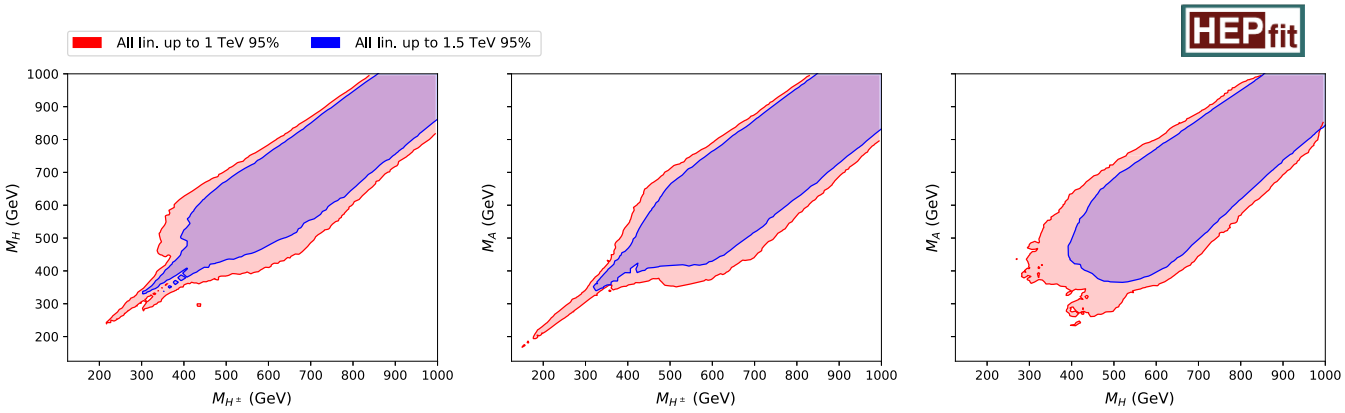

FIG. 8. Correlations among the masses of the new scalars.

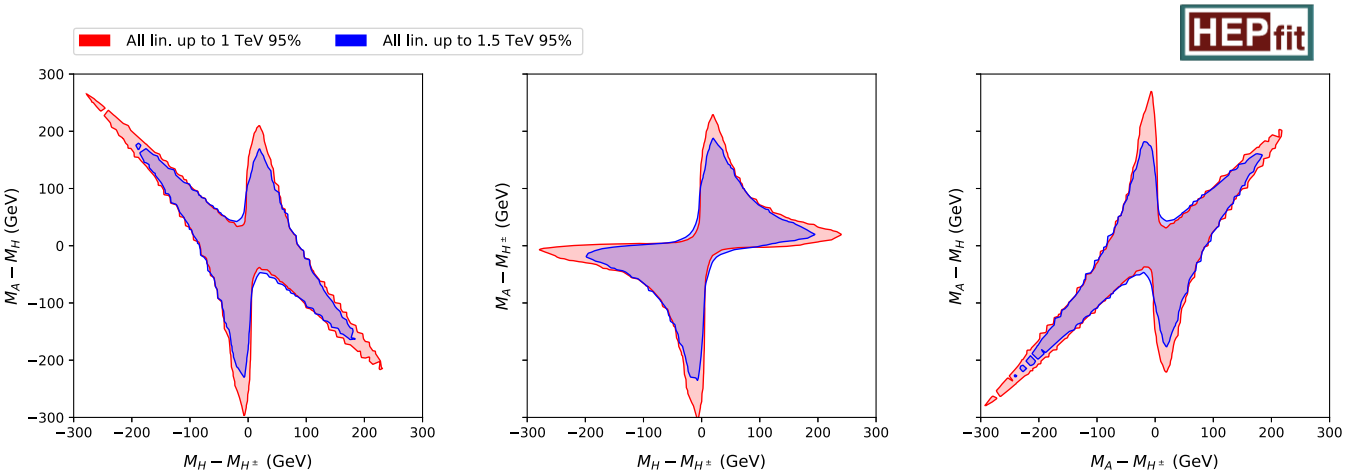

FIG. 9. Correlations among the mass splittings.

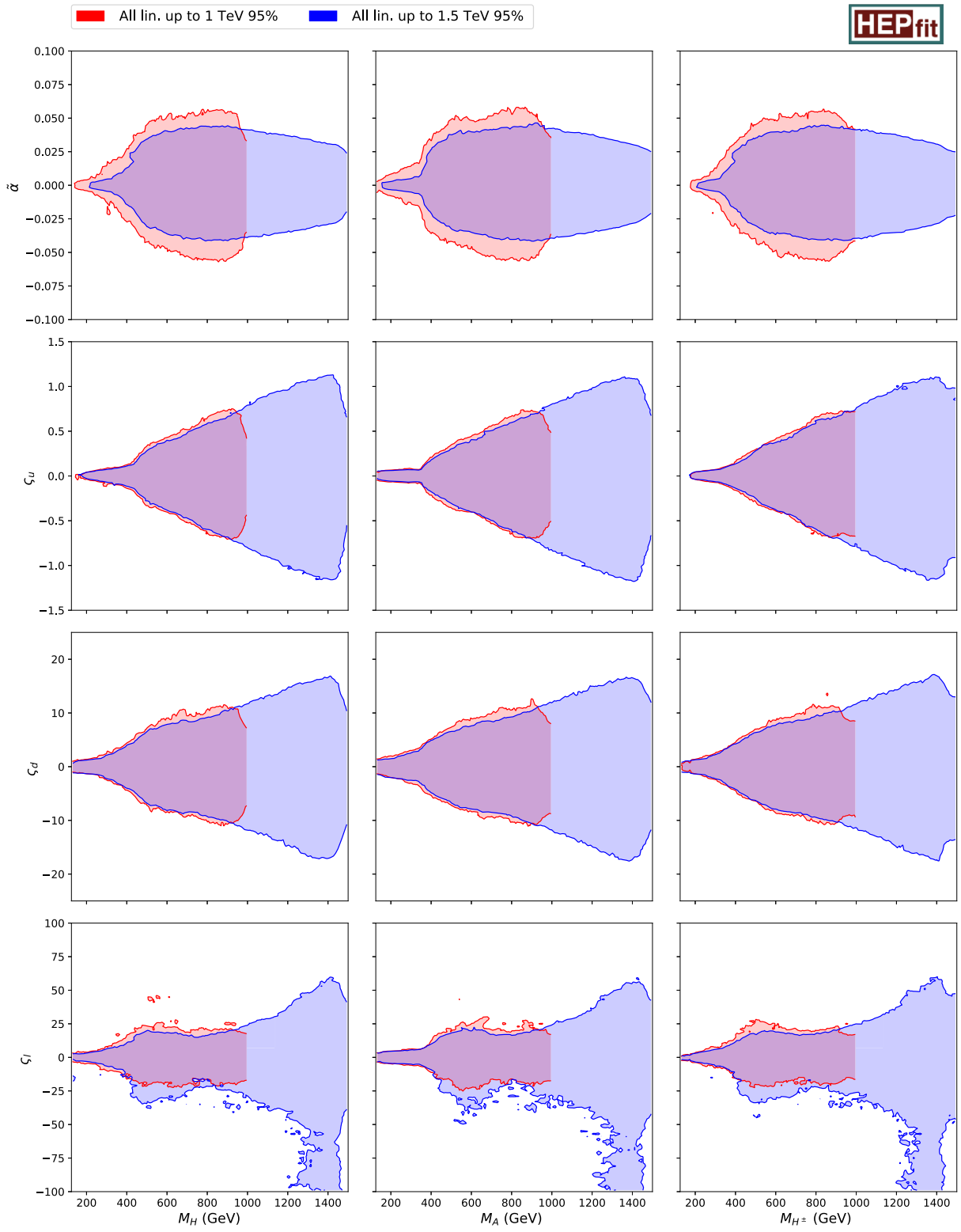

FIG. 10. Correlations among the mixing angle and the Yukawa alignment parameters with the masses.

again, this behavior is generated by the oblique parameters, whose NP contribution tends to zero when the mass splitting between any neutral scalar and the charged scalar vanishes. The last interesting plots regarding the masses are their correlations with the Yukawa alignment parameters and the mixing angle, shown in Fig. 10. Here we can see how the higher the masses get, the higher the Yukawa alignment parameters can be. Nevertheless, for masses

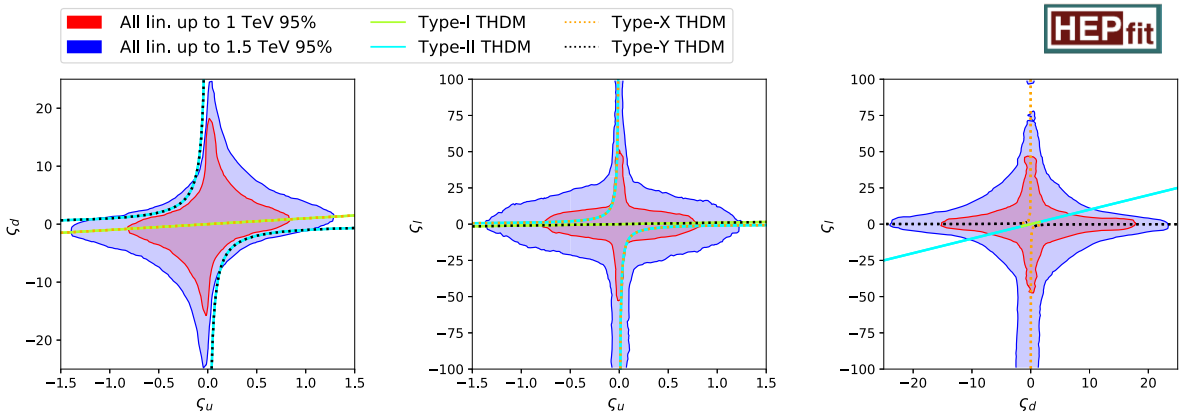

FIG. 11. Correlations among the Yukawa alignment parameters. Also shown are the restrictions (2.18) imposed in the different $\mathcal{Z}_2$ THDMs (the inert model is omitted since in that case these couplings are simply set to zero).

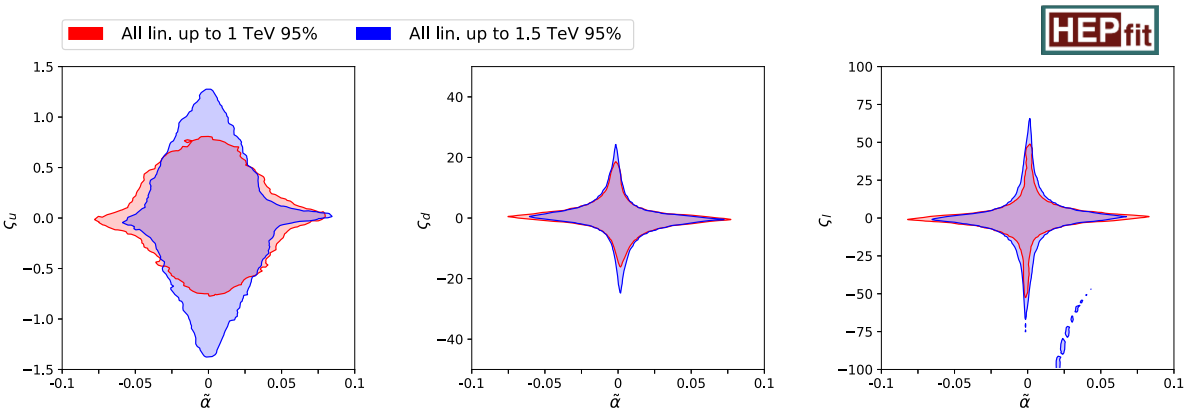

FIG. 12. Correlations among the mixing angle and the Yukawa alignment parameters.

above 700 GeV, smaller values of the mixing angle are preferred due to the theoretical constraints, as explained before. Finally, for very small values of the Yukawa alignment parameters or the mixing angle the limits on the masses also start to disappear, as expected.

The correlations of the Yukawa alignment parameters among themselves and with the mixing angle are shown in Figs. 11 and 12, respectively. In the first one we observe that the regions get wider when higher masses are allowed, since all experimental constraints become softer, as also shown in Fig. 10. Moreover, once one of the Yukawa alignment parameters tends to high values, the others get highly suppressed. Indeed, for masses up to 1 TeV, in order to obtain values of ς_d or ς_l of order 10, ς_u must be of order 0.1 or smaller. We observe a similar behavior by looking at the correlations of the Yukawa alignment parameters with the mixing angle. The higher the mixing angle, the smaller the Yukawa alignment parameters must be, and the higher the allowed range of masses, the higher the Yukawa alignment parameters can be. However, as can also be seen in Fig. 10, the mixing angle does not grow with the masses, and slightly smaller values of $\tilde{\alpha}$ are preferred when heavier masses are allowed in the fit. Nevertheless, performing a fit with a wider mass region does not significantly change the shape of the correlations between the Yukawa alignment parameters and the mixing angle with respect to the masses of the scalars. Integrating over the masses, like in Figs. 11 and 12, the shape stays basically unchanged and just rescales when a different mass range is covered. Indeed, performing the fits for these two different mass ranges allows us to get an idea of the shape of the multidimensional correlation of the masses against the other parameters which, unfortunately, cannot be printed in a two-dimensional plot.

In Fig. 11 we also show the restrictions [Eq. (2.18)] each $\mathcal{Z}_2$ THDM would impose on the Yukawa alignment couplings. In these models, all alignment parameters are related through an angle β, whose tangent measures the ratio of the VEVs of the two scalar fields in the basis where the discrete $\mathcal{Z}_2$ symmetry is imposed. Therefore, each $\mathcal{Z}_2$-symmetric model corresponds to specific curves (either straight lines or hyperbolas) in the $\varsigma_{f_1} - \varsigma_{f_2}$ planes, each point of which represents different values of $\tan\beta$. The curves in green (thick solid), cyan (thin solid), orange

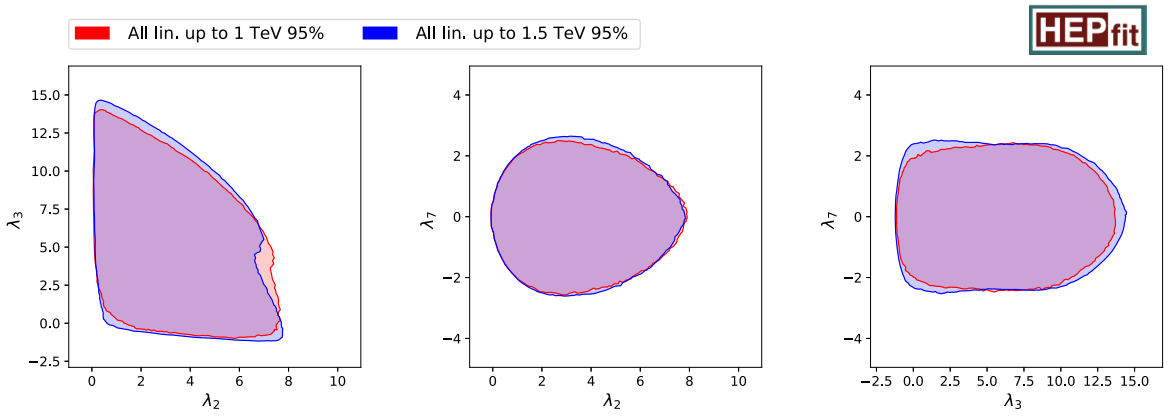

FIG. 13. Correlations among the quartic couplings.

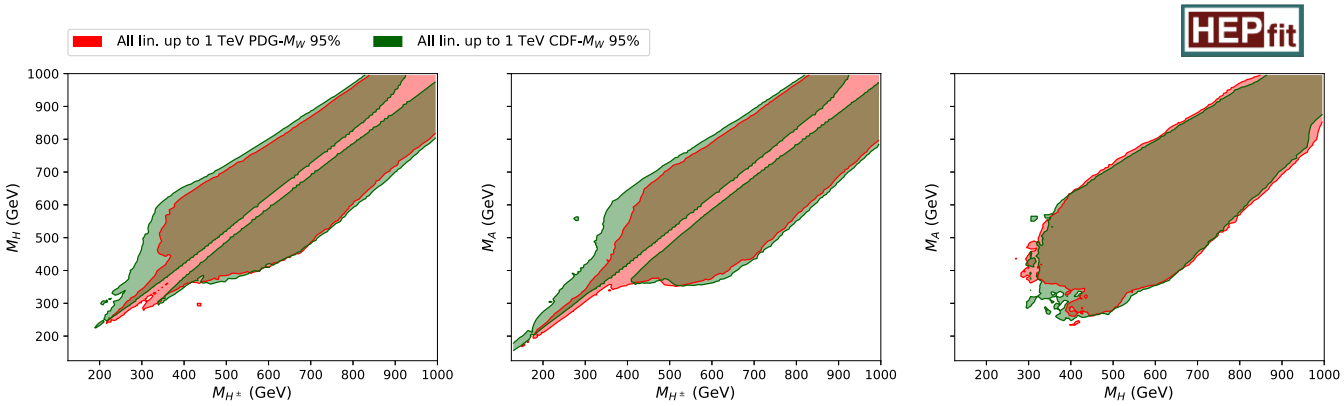

FIG. 14. Correlations among the masses of the new scalars, with and without including the CDF measurement of M_W.

(thin dotted), and black (thick dotted) depict the type-I, type-II, type-X, and type-Y THDMs, respectively, whereas the inert THDM corresponds to an isolated point at the origin. The first panel in Fig. 11 indicates that the type-II and type-Y models have some tension with the (mainly flavor) data. Note, however, that this is just a qualitative comparison. In order to analyze the parameter space of any of these particular models, we would need to change the priors of our analysis by considering $\tan\beta$ as the free parameter instead of the alignment parameters along with the constraint $\mu_3 = \lambda_6 = \lambda_7 = 0$. A comprehensive investigation of the parameter space for each of these models, though valuable, falls outside the scope of this study. We refer the interested reader to the more recent specific analyses in Refs. [49,50].

Finally, in Fig. 13 we plot the correlations among the quartic couplings of the scalar potential. These couplings are mainly constrained by the theoretical bounds (perturbative unitarity, boundedness from below, and vacuum stability) and therefore their constraints do not depend on the mass range studied. Indeed, these limits are approximately the same as those of Fig. 2, in which only the theoretical considerations have been taken into account.

D. CDF W-mass measurement

As mentioned before, in 2022 the CDF Collaboration released a new measurement of the mass of the W boson [78] with a 7σ tension with the SM prediction. Since there is still a controversy in the community, we do not include this last measurement in our main analysis, but we provide here the results of a global fit including that information. In particular, we take the values of the oblique parameters (S and T) from Ref. [103]. Using that data as an input, we obtain a posterior value for $M_W = 80.4178 \pm 0.0091$ GeV which is compatible with the CDF measurement ($M_W^{\rm CDF} = 80.433 \pm 0.009$) within a 95% probability. The additional scalars of the ATHDM would then be able to explain this result, if confirmed.[9] As can be seen in Figs. 14 and 15, in order to generate this additional contribution to M_W we need a mass difference among the charged scalar and the neutral scalars of, at least, a few tens of GeV. Besides this mass difference, the results for the other parameters are very similar to the ones obtained in the baseline fit, as expected.

[9]Of course, we are not able to explain the 4σ incompatibility between the ATLAS [122,123] and CDF [78] measurements.

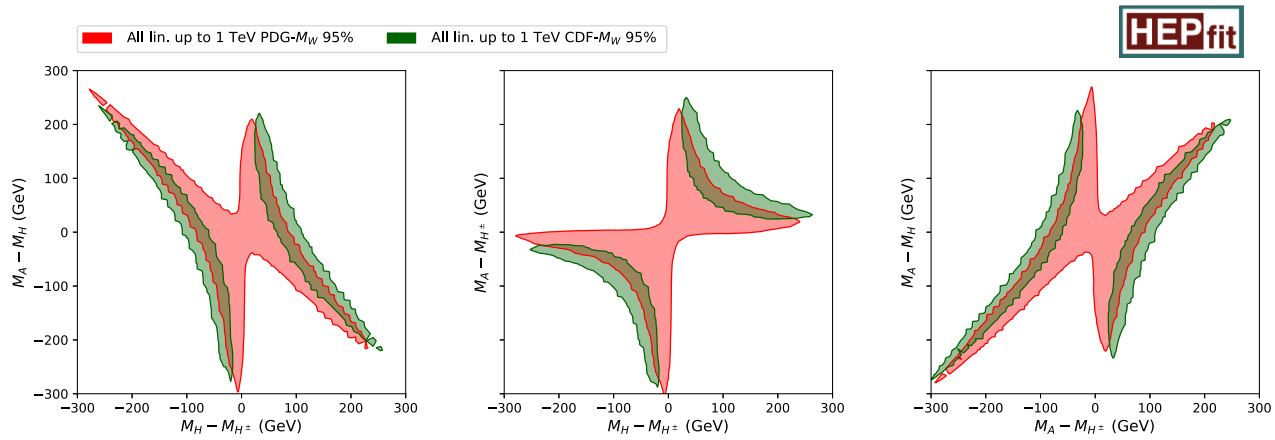

FIG. 15. Correlations among the scalar mass splittings, with and without including the CDF measurement of M_W.

VI. CONCLUSION

In this work we have performed an extensive phenomenological analysis of the *CP*-conserving ATHDM, using the HEPfit package. These results update the previous work of Ref. [74],[10] although here we used a slightly different set of parameters. The observed SM Higgs boson at a mass of 125 GeV has been assumed to be the lightest scalar particle, and therefore we focused our study on heavy NP scalars. More details on the region of the parameter space that we scanned can be found in Sec. III.

We incorporated the theoretical requirements of perturbative unitarity, boundedness of the scalar potential from below, and vacuum stability, and the most relevant experimental constraints, including direct searches at the LHC, Higgs signal strengths, electroweak precision observables, and flavor data. The main results of the global fit, combining all theoretical and experimental constraints at the same time, are shown in Sec. V C.

We had a total of ten NP parameters to fit. Three of them are the Yukawa alignment parameters for up-type quarks (ς_u), down-type quarks (ς_d), and leptons (ς_l). The other seven come from the scalar potential, where we chose the three heavy scalar masses (M_H, M_A, and $M_{H^\pm}$), the mixing angle among the neutral scalars ($\tilde{\alpha}$), and three quartic couplings (λ_2, λ_3, and λ_7). The only relevant constraints on these quartic couplings come from theoretical considerations. The mixing angle is mainly constrained by the Higgs signal strengths and lower limits on the masses of the new scalars were obtained from direct searches and flavor observables (which constrain the mass of the charged scalar). The mass difference among the charged scalar and (at least one of) the neutral scalars is highly constrained by the oblique parameters. The theoretical requirements also provide relevant constraints on the mass splittings and the mixing angle for high values of the charged scalar mass. Finally, the Yukawa alignment parameters are mainly constrained by the direct searches and flavor observables.

The marginalized probabilities for all of the parameters can be found in Table II. In this table, we show results for a fit in which the scan on the masses is done up to 1 TeV and one in which the scan is done up to 1.5 TeV. These ranges of masses were chosen according to the ranges testable at the LHC. Obviously, the results differ according to the range considered, since higher masses are always favored. Note also that the lower bounds on the masses are highly correlated with the values of the Yukawa alignment parameters. If we set these parameters to sufficiently low values, the constraints on the masses vanish. For masses up to 1 TeV, values of $|\varsigma_u| > 0.7$, $|\varsigma_d| > 12$, $|\varsigma_l| > 30$, and $|\tilde{\alpha}| > 0.06$ are outside of the 95% probability region.

Besides performing this global fit with the state-of-the-art data, we also studied two additional measurements that, at the moment, deviate from the SM prediction: the muon $(g-2)$ [118,119] and the new measurement of M_W from the CDF Collaboration [78]. In both cases we did not include them in the global fit because they are still controversial, although for different reasons. Nevertheless, we have shown that the ATHDM has enough flexibility to accommodate both measurements within its parameter space, while still being compatible with all other constraints.

ACKNOWLEDGMENTS

We thank the developers of the previous global fit to this model, Otto Eberhardt and Ana Peñuelas. We also thank Luca Silvestrini, Ayan Paul, and Antonio Coutinho for some useful discussions and technical support regarding HEPfit. This work has been supported in part by Generalitat Valenciana (Grant PROMETEO/2021/071) and by MCIN/AEI/10.13039/501100011033 (Grant No. PID2020–114473GB-I00). The work of V. M. has been supported by the Italian Ministry of Research (MUR) under the grant PRIN20172LNEEZ.

[10]In this work, we have adopted as baseline the same code used in Ref. [74], but we also included some relevant modifications. We thank the developers of the previous version who are not signing this paper: O. Eberhardt and A. Peñuelas.

APPENDIX A: DATA INCLUDED

The following tables compile all experimental references included in the fit for the direct searches and the Higgs signal strengths.

TABLE III. Higgs signal strengths measured by ATLAS and CMS. Note that not all of the decays have been measured for all of the production channels.

		References	L [fb^{-1}]	$\sqrt{s}$ [TeV]	References	L [fb^{-1}]	$\sqrt{s}$ [TeV]
Production	Decay	ATLAS			CMS		
	$c\bar{c}$	[124]	139	13	[125]	35.9	13
	$b\bar{b}$	[126,127]	4.7/20.3	7/8	[128,129]	5.1/18.9	7/8
		[101,130,131]	126/139	13	[101,132,133]	2.3/41.3	13
ggF	$\gamma\gamma$	[134]	4.5/20.3	7/8	[135]	5.1/19.7	7/8
		[136]	139	13	[137]	137	13
VBF	$\mu^+\mu^-$	[138]	5/20	7/8	[138]	5/20	7/8
		[139]	139	13	[140]	137	13
Vh	$\tau^+\tau^-$	[141]	4.5/20.3	7/8	[142]	4.9/19.7	7/8
		[143]	139	13	[144]	137	13
tth	WW	[145,146]	25, 4.5/20.3	7/8	[147]	4.9/19.4	7/8
		[143]	139	13	[144]	137	13
	$Z\gamma$	[148]	4.7/20.3	7/8	[149]	5/19.6	7/8
		[150]	139	13	[151]	35.9	13
	ZZ	[152]	4.5/20.3	7/8	[153]	5.1/19.7	7/8
		[154]	139	13	[144]	137	13

TABLE IV. Direct searches for charged scalars.

Label	Channel	Experiment		Mass range [TeV]	$\mathcal{L}$ [fb^{-1}]
$A_8^{\tau\nu}$	$pp \to H^\pm \to \tau^\pm\nu$	ATLAS	[155]	[0.18;1]	19.5
$C_8^{\tau\nu}$	$pp \to H^\pm \to \tau^\pm\nu$	CMS	[156]	[0.18;0.6]	19.7
$A_{13}^{\tau\nu}$	$pp \to H^\pm \to \tau^\pm\nu$	ATLAS	[157]	[0.09;2]	36.1
$C_{13}^{\tau\nu}$		CMS	[158]	[0.08;3]	35.9
A_8^{tb}	$pp \to H^\pm \to tb$	ATLAS	[159]	[0.2;0.6]	20.3
C_8^{tb}	$pp \to H^\pm \to tb$	CMS	[156]	[0.18;0.6]	19.7
A_{13}^{tb}	$pp \to H^\pm \to tb$	ATLAS	[160]	[0.2;2]	139
C_{13}^{tb}		CMS	[161]	[0.2;3]	35.9

TABLE V. Direct searches for neutral heavy scalars, $\varphi_i^0 = H, A$, with final states including the SM Higgs boson or other neutral scalars. φ_3 denotes the heaviest scalar, $V = W, Z$, $\ell = e, \mu$. Parentheses show the final decay of the SM particles produced from the NP particles. Square brackets are used when the values of $\sigma \cdot \mathcal{B}$ are shown in terms of the primary decay (i.e., the NP particle decay) but a particular decay channel of the SM particles is used to obtain those values. See Sec. IV B for more details.

Label	Channel	Experiment		Mass range [TeV]	$\mathcal{L}$ [fb^{-1}]
A_8^{hh}	$gg \to \varphi_i^0 \to hh$	ATLAS	[162]	[0.26;1]	20.3
C_8^{4b}	$pp \to \varphi_i^0 \to hh \to (bb)(bb)$	CMS	[163]	[0.27;1.1]	17.9
$C_8^{2\gamma 2b}$	$pp \to \varphi_i^0 \to hh \to (bb)(\gamma\gamma)$	CMS	[164]	[0.260;1.1]	19.7
$C_{8g}^{2b2\tau}$	$gg \to \varphi_i^0 \to hh \to (bb)(\tau\tau)$	CMS	[165]	[0.26;0.35]	19.7
$C_8^{2b2\tau}$	$pp \to \varphi_i^0 \to hh[\to (bb)(\tau\tau)]$	CMS	[166]	[0.35;1]	18.3

(Table continued)

TABLE V. *(Continued)*

Label	Channel	Experiment		Mass range [TeV]	$\mathcal{L}$ [fb^{-1}]
A_{13}^{4b}	$pp \to \varphi_i^0 \to hh \to (bb)(bb)$	ATLAS	[167]	[0.251;5]	139
$C_{13,1}^{4b}$		CMS	[168]	[0.26;1.2]	35.9
$C_{13,2}^{4b}$		CMS	[169]	[1;3]	138
C_{13}^{4W}	$pp \to \varphi_i^0 \to hh \to (WW)(WW)/(WW)(\tau\tau)/(\tau\tau)(\tau\tau)$	CMS	[170]	[0.25;1]	138
$A_{13}^{2\gamma 2b}$	$pp \to \varphi_i^0 \to hh[\to (bb)(\gamma\gamma)]$	ATLAS	[171]	[0.251;1]	139
$C_{13}^{2\gamma 2b}$	$pp \to \varphi_i^0 \to hh \to (bb)(\gamma\gamma)$	CMS	[172]	[0.25;0.9]	35.9
$A_{13,1}^{2b2\tau}$	$pp \to \varphi_i^0 \to hh \to (bb)(\tau\tau)$	ATLAS	[173]	[0.251;1.6]	139
$A_{13,1}^{2b2\tau}$		ATLAS	[174]	[1;3]	139
$C_{13,1}^{2b2\tau}$	$pp \to \varphi_i^0 \to hh[\to (bb)(\tau\tau)]$	CMS	[175]	[0.25;0.9]	35.9
$C_{13,2}^{2b2\tau}$		CMS	[176]	[0.9;4]	35.9
C_{13}^{2b2V}	$pp \to \varphi_i^0 \to hh \to (bb)(VV \to \ell\nu\ell\nu)$	CMS	[177]	[0.26;0.9]	35.9
C_{13}^{2b2W}	$pp \to \varphi_i^0 \to hh \to (bb)(WW \to q\bar{q}\ell\nu)$	CMS	[178]	[0.8;3.5]	35.9
C_{13}^{2b2Z}	$pp \to \varphi_i^0 \to hh \to (bb)(ZZ \to \ell\ell jj)$	CMS	[179]	[0.26;1]	35.9
C_{13}^{2b2Z}	$pp \to \varphi_i^0 \to hh \to (bb)(ZZ \to \ell\ell\nu\nu)$	CMS	[179]	[0.26;1]	35.9
A_{13}^{2b2W}	$pp \to \varphi_i^0 \to hh[\to (bb)(WW)]$	ATLAS	[180]	[0.5;3]	36.1
C_{13}^{2b2W}	$pp \to \varphi_i^0 \to hh[\to (bb)(WW/\tau\tau \to (q\bar{q}/\ell\nu)\ell\nu)]$	CMS	[181]	[0.8;4.5]	138
$A_{13}^{2\gamma 2W}$	$gg \to \varphi_i^0 \to hh \to (\gamma\gamma)(WW)$	ATLAS	[182]	[0.26;0.5]	36.1
A_{8}^{bbZ}	$gg \to \varphi_i^0 \to hZ \to (bb)Z$	ATLAS	[183]	[0.22;1]	20.3
$C_{8}^{2b2\ell}$	$gg \to \varphi_i^0 \to hZ \to (bb)(\ell\ell)$	CMS	[184]	[0.225;0.6]	19.7
$A_{8}^{\tau\tau Z}$	$gg \to \varphi_i^0 \to hZ \to (\tau\tau)Z$	ATLAS	[183]	[0.22;1]	20.3
$C_{8}^{2\tau 2\ell}$	$gg \to \varphi_i^0 \to hZ \to (\tau\tau)(\ell\ell)$	CMS	[165]	[0.22;0.35]	19.7
A_{13}^{bbZ}	$gg \to \varphi_i^0 \to hZ \to (bb)Z$	ATLAS	[185]	[0.2;2]	36.1
$C_{13,1}^{bbZ}$		CMS	[186]	[0.22;0.8]	35.9
$C_{13,2}^{bbZ}$		CMS	[187]	[0.8;2]	35.9
$C_{13,3}^{bbZ}$	$gg \to \varphi_i^0 \to (h \to \tau\tau)(Z \to \ell\ell)$	CMS	[188]	[0.22;0.4]	35.9
A_{13b}^{bbZ}	$bb \to \varphi_i^0 \to hZ \to (bb)Z$	ATLAS	[185]	[0.2;2]	36.1
$C_{13b,1}^{bbZ}$		CMS	[186]	[0.22;0.8]	35.9
$C_{13b,2}^{bbZ}$		CMS	[187]	[0.8;2]	35.9
$C_{8,1}^{\varphi_2^0 Z}$	$pp \to \varphi_3^0 \to \varphi_2^0 Z \to (bb)(\ell\ell)$	CMS	[189]	[0.04;1]	19.8
$C_{8,2}^{\varphi_2^0 Z}$	$pp \to \varphi_3^0 \to \varphi_2^0 Z \to (\tau\tau)(\ell\ell)$	CMS	[189]	[0.05;1]	19.8
$A_{13}^{\varphi^0 Z}$	$gg \to \varphi_3^0 \to \varphi_2^0 Z \to (bb)Z$	ATLAS	[190]	[0.13/0.23;0.7/0.8]	139
$A_{13b}^{\varphi^0 Z}$	$bb \to \varphi_3^0 \to \varphi_2^0 Z \to (bb)Z$	ATLAS	[190]	[0.13/0.23;0.7/0.8]	139

TABLE VI. Direct searches for neutral heavy scalars, $\varphi_i^0 = H$, A, with quarks, leptons ($\ell = e$, μ), photons and $Z\gamma$ final states. Parentheses show the final decay of the SM particles produced from the NP particles. Square brackets are used when the values of $\sigma \cdot \mathcal{B}$ are shown in terms of the primary decay (i.e., the NP particle decay) but a particular decay channel of the SM particles is used to obtain those values. See Sec. IV B for more details.

Label	Channel	Experiment		Mass range [TeV]	$\mathcal{L}$ [fb^{-1}]
A_{13b}^{tt}	$bb \to \varphi_i^0 \to tt$	ATLAS	[191]	[0.4;1]	13.2
C_{13t}^{tt}	$tt/tW/tq \to \varphi_i^0 \to tt$	CMS	[192]	[0.35;0.65]	137
A_{13t}^{tt}	$tt \to \varphi_i^0 \to tt$	ATLAS	[193]	[0.4;1]	137
C_{8b}^{bb}	$bb \to \varphi_i^0 \to bb$	CMS	[194]	[0.1;0.9]	19.7
C_{8}^{bb}	$gg \to \varphi_i^0 \to bb$	CMS	[195]	[0.33;1.2]	19.7

(Table continued)

TABLE VI. *(Continued)*

Label	Channel	Experiment		Mass range [TeV]	$\mathcal{L}$ [fb^{-1}]
C_{13}^{bb}	$pp \to \varphi_i^0 \to bb$	CMS	[196]	[0.55;1.2]	2.69
C_{13b}^{bb}	$bb \to \varphi_i^0 \to bb$	CMS	[197]	[0.3;1.3]	35.7
A_{13}^{bb}	$pp \to \varphi_i^0 \to bb$ (≥ 1 b-jet)	ATLAS	[198]	[1.4;6.6]	36.1
A_{13}^{bb}	$pp \to \varphi_i^0 \to bb$	ATLAS	[198]	[0.6;1.25]	24.3
A_{13}^{bb}	$pp \to \varphi_i^0 \to bb$	ATLAS	[198]	[1.25;6.2]	36.1
A_{13b}^{bb}	$bb \to \varphi_i^0 \to bb$	ATLAS	[199]	[0.45;1.4]	27.8
C_{13}^{bb}	$pp \to \varphi_i^0 \to bb$	CMS	[200]	[0.05;0.35]	35.9
$C_{8b}^{\mu\mu}$	$bb \to \varphi_i^0 \to \mu\mu$	CMS	[201]	[0.12;0.5]	19.3
$C_{8}^{\mu\mu}$	$gg \to \varphi_i^0 \to \mu\mu$	CMS	[201]	[0.12;0.5]	19.3
$C_{13b}^{\mu\mu}$	$bb \to \varphi_i^0 \to \mu\mu$	CMS	[202]	[0.14;1]	35.9
$C_{13}^{\mu\mu}$	$gg \to \varphi_i^0 \to \mu\mu$	CMS	[202]	[0.14;1]	35.9
$A_{13b}^{\mu\mu}$	$bb \to \varphi_i^0 \to \mu\mu$	ATLAS	[203]	[0.2;1]	36.1
$A_{13}^{\mu\mu}$	$gg \to \varphi_i^0 \to \mu\mu$	ATLAS	[203]	[0.2;1]	36.1
$A_{8}^{\tau\tau}$	$gg \to \varphi_i^0 \to \tau\tau$	ATLAS	[204]	[0.09;1]	20
$C_{8}^{\tau\tau}$		CMS	[205]	[0.09;1]	19.7
$A_{8b}^{\tau\tau}$	$bb \to \varphi_i^0 \to \tau\tau$	ATLAS	[204]	[0.09;1]	20
$C_{8b}^{\tau\tau}$		CMS	[205]	[0.09;1]	19.7
$A_{13}^{\tau\tau}$	$gg \to \varphi_i^0 \to \tau\tau$	ATLAS	[206]	[0.2;1.2]	3.2
$A_{13b}^{\tau\tau}$	$bb \to \varphi_i^0 \to \tau\tau$	ATLAS	[206]	[0.2;1.2]	3.2
$A_{13}^{\tau\tau}$	$gg \to \varphi_i^0 \to \tau\tau$	ATLAS	[207]	[0.2;2.5]	139
$A_{13b}^{\tau\tau}$	$bb \to \varphi_i^0 \to \tau\tau$	ATLAS	[207]	[0.2;2.5]	139
$C_{13}^{\tau\tau}$	$gg \to \varphi_i^0 \to \tau\tau$	CMS	[208]	[0.06;3.5]	138
$C_{13b}^{\tau\tau}$	$bb \to \varphi_i^0 \to \tau\tau$	CMS	[208]	[0.06;3.5]	138
$A_{13}^{\tau\tau}$	$gg \to \varphi_i^0 \to \tau\tau$	ATLAS	[209]	[0.2;2.25]	36.1
$C_{13}^{\tau\tau}$		CMS	[210]	[0.09;3.2]	35.9
$A_{13b}^{\tau\tau}$	$bb \to \varphi_i^0 \to \tau\tau$	ATLAS	[209]	[0.2;2.25]	36.1
$C_{13b}^{\tau\tau}$		CMS	[210]	[0.09;3.2]	35.9
$A_{8}^{\gamma\gamma}$	$gg \to \varphi_i^0 \to \gamma\gamma$	ATLAS	[211]	[0.065;0.6]	20.3
$C_{13}^{\gamma\gamma}$	$gg \to \varphi_i^0 \to \gamma\gamma$	CMS	[212]	[0.5;4]	35.9
$C_{13}^{\gamma\gamma}$	$gg \to \varphi_i^0 \to \gamma\gamma$	CMS	[213]	[0.5;5]	35.9
$A_{13}^{\gamma\gamma}$	$pp \to \varphi_i^0 \to \gamma\gamma$	ATLAS	[214]	[0.15;3]	139
$A_{8}^{Z\gamma}$	$pp \to \varphi_i^0 \to Z\gamma \to (\ell\ell)\gamma$	ATLAS	[215]	[0.2;1.6]	20.3
$C_{8}^{Z\gamma}$		CMS	[216]	[0.2;1.2]	19.7
$C_{13}^{\ell\ell\gamma}$	$pp \to \varphi_i^0 \to Z\gamma[\to (\ell\ell)\gamma]$	CMS	[217]	[0.35;4]	35.9
$C_{13}^{qq\gamma}$	$pp \to \varphi_i^0 \to Z\gamma[\to (qq)\gamma]$	CMS	[217]	[0.35;4]	35.9
$C_{13}^{Z\gamma}$	$pp \to \varphi_i^0 \to Z\gamma[\to (\ell\ell \,\&\, qq)\gamma]$	CMS	[217]	[0.35;4]	35.9
$A_{13}^{\ell\ell\gamma}$	$gg \to \varphi_i^0 \to Z\gamma[\to (\ell\ell)\gamma]$	ATLAS	[218]	[0.25;2.4]	36.1
$A_{13}^{qq\gamma}$	$gg \to \varphi_i^0 \to Z\gamma[\to (qq)\gamma]$	ATLAS	[219]	[1;6.8]	36.1
$C_{8+13}^{Z\gamma}$	$gg \to \varphi_i^0 \to Z\gamma$	CMS	[217]	[0.35;4]	35.9

TABLE VII. Direct searches for neutral heavy scalars, $\varphi_i^0 = H, A$, with vector-boson final states. $V = W, Z$, $\ell = e, \mu$. Parentheses show the final decay of the SM particles produced from the NP particles. Square brackets are used when the values of $\sigma \cdot \mathcal{B}$ are shown in terms of the primary decay (i.e., the NP particle decay) but a particular decay channel of the SM particles is used to obtain those values. See Sec. IV B for more details.

Label	Channel	Experiment		Mass range [TeV]	$\mathcal{L}$ [fb^{-1}]
A_8^{ZZ}	$gg \to \varphi_i^0 \to ZZ$	ATLAS	[220]	[0.14;1]	20.3
A_{8V}^{ZZ}	$VV \to \varphi_i^0 \to ZZ$	ATLAS	[220]	[0.14;1]	20.3
$A_{13}^{2\ell 2L}$	$gg \to \varphi_i^0 \to ZZ[\to (\ell\ell)(\ell\ell,\nu\nu)]$	ATLAS	[221]	[0.2;1.2]	36.1
$A_{13V}^{2\ell 2L}$	$VV \to \varphi_i^0 \to ZZ[\to (\ell\ell)(\ell\ell,\nu\nu)]$	ATLAS	[221]	[0.2;1.2]	36.1
$A_{13}^{2\ell 2L}$	$gg \to \varphi_i^0 \to ZZ[\to (\ell\ell)(\ell\ell,\nu\nu)]$	ATLAS	[222]	[0.2;2]	139
$A_{13V}^{2\ell 2L}$	$VV \to \varphi_i^0 \to ZZ[\to (\ell\ell)(\ell\ell,\nu\nu)]$	ATLAS	[222]	[0.2;2]	139
A_{13}^{2L2q}	$gg \to \varphi_i^0 \to ZZ[\to (\ell\ell,\nu\nu)(qq)]$	ATLAS	[223]	[0.3;3]	36.1
A_{13V}^{2L2q}	$VV \to \varphi_i^0 \to ZZ[\to (\ell\ell,\nu\nu)(qq)]$	ATLAS	[223]	[0.3;3]	36.1
$C_{13}^{2\ell 2X}$	$pp \to \varphi_i^0 \to ZZ[\to (\ell\ell)(qq,\nu\nu,\ell\ell)]$	CMS	[224]	[0.13;3]	35.9
$C_{13}^{2q2\nu}$	$pp \to \varphi_i^0 \to ZZ[\to (qq)(\nu\nu)]$	CMS	[225]	[1;4]	35.9
A_8^{WW}	$gg \to \varphi_i^0 \to WW$	ATLAS	[226]	[0.3;1.5]	20.3
A_{8V}^{WW}	$VV \to \varphi_i^0 \to WW$	ATLAS	[226]	[0.3;1.5]	20.3
C_{13V}^{WW}	$VV \to \varphi_i^0 \to WW$	CMS	[227]	[0.2;3]	35.9
$A_{13}^{2(\ell\nu)}$	$gg \to \varphi_i^0 \to WW[\to (e\nu)(\mu\nu)]$	ATLAS	[228]	[0.2;4]	36.1
$A_{13V}^{2(\ell\nu)}$	$VV \to \varphi_i^0 \to WW[\to (e\nu)(\mu\nu)]$	ATLAS	[228]	[0.2;3]	36.1
$C_{13}^{2(\ell\nu)}$	$(gg + VV) \to \varphi_i^0 \to WW \to (\ell\nu)(\ell\nu)$	CMS	[229]	[0.2;1]	2.3
$A_{13}^{\ell\nu 2q}$	$gg \to \varphi_i^0 \to WW[\to (\ell\nu)(qq)]$	ATLAS	[230]	[0.3;3]	36.1
$A_{13V}^{\ell\nu 2q}$	$VV \to \varphi_i^0 \to WW[\to (\ell\nu)(qq)]$	ATLAS	[230]	[0.3;3]	36.1
$C_{13}^{\ell\nu 2q}$	$pp \to \varphi_i^0 \to WW[\to (\ell\nu)(qq)]$	CMS	[231]	[1;4.4]	35.9
C_8^{VV}	$pp \to \varphi_i^0 \to VV$	CMS	[232]	[0.145;1]	24.8
A_{13}^{4q}	$pp \to \varphi_i^0 \to VV[\to (qq)(qq)]$	ATLAS	[233]	[1.2;3]	36.7
A_{13}^{VV}	$pp \to \varphi_i^0 \to VV$	ATLAS	[234]	[0.3;3]	36.1
A_{13V}^{VV}	$VV \to \varphi_i^0 \to VV$	ATLAS	[234]	[0.3;3]	36.1
A_{13}^{VV}	$gg \to \varphi_i^0 \to VV$	ATLAS	[235]	[0.2;5.2]	139
A_{13V}^{VV}	$VV \to \varphi_i^0 \to VV$	ATLAS	[235]	[0.2;5.2]	139
C_{13}^{WW}	$gg \to \varphi_i^0 \to WW$	CMS	[236]	[1,4.5]	137
C_{13V}^{WW}	$VV \to \varphi_i^0 \to WW$	CMS	[236]	[1;4.5]	137

APPENDIX B: NONCONTAMINATED STANDARD MODEL INPUTS

In this work we include as inputs the entries of the CKM matrix, in the Wolfenstein parametrization [104], and the oblique parameters [96,97]. The experimental values of these parameters quoted by the PDG [101] have been obtained through an SM fit of multiple observables, neglecting any NP contributions. Unfortunately, this assumption is not satisfied in our model for all of the observables included in the fits, and we need to repeat these fits without the problematic observables.

1. Noncontaminated CKM fit

We extract the Wolfenstein parameters from the measured values of the CKM matrix elements (or ratios among them).

a. Determination of $|V_{ud}|$

For $|V_{ud}|$ we use directly the value quoted by the PDG [101],

$$|V_{ud}| = 0.97373 \pm 0.00031, \tag{B1}$$

since this value comes from superallowed $0^+ \to 0^+$ nuclear β decays [237] with completely negligible contamination from our additional scalars.

b. Determination of $|V_{us}|$

The determination of $|V_{us}|$ in the PDG [101] is based on semileptonic decays of kaons, averaging the electronic and muonic channels, and, independently, on the pure leptonic decay of kaons and pions to muons which provide the ratio $|V_{us}/V_{ud}|$. The scalar contribution to the semileptonic decays is highly suppressed by the light lepton masses. Therefore, as long as the mass of the kaons is much higher than the mass of the decaying lepton we can safely neglect the NP contribution in the semileptonic decays. This assumption holds for the semileptonic decay to electrons but it is not fulfilled for the muonic channel. Therefore, for the semileptonic decays we only consider the decays to electrons, including the K_L, K_S, and K^+ decays, which give the average value $|V_{us} f_+^K(0)| = 0.21626 \pm 0.00040$ [238]. Taking the form-factor average $f_+(0) = 0.9698 \pm 0.0017$ from $N_f = 2+1+1$ lattice QCD calculations [239] gives $|V_{us}| = 0.2230 \pm 0.0006$.

As mentioned above, the alternative determination of $|V_{us}|$ is based on the leptonic kaon decay. In this case, the SM contribution is helicity suppressed, making the scalar contribution relatively much higher. In general, the charged-scalar contribution to the leptonic decay of a pseudoscalar-meson takes the form [37]

$$\Gamma(P_{ij}^+ \to l^+ \nu_l) = \Gamma^{\rm SM}(P_{ij}^+ \to l^+ \nu_l)|1 - \Delta_{ij}|^2, \tag{B2}$$

where i, j are the flavor indices corresponding to the valence quarks of the meson, the NP correction

$$\Delta_{ij} = \left(\frac{m_{P_{ij}^+}}{M_{H^\pm}}\right)^2 \varsigma_l^* \frac{\varsigma_u m_{ui} + \varsigma_d m_{dj}}{m_{ui} + m_{dj}}, \tag{B3}$$

and the SM contribution is related to the CKM matrix element by

$$\Gamma^{\rm SM}(P_{ij}^+ \to l^+ \nu_l) = G_F^2 m_l^2 f_P^2 |V_{ij}|^2 \frac{m_{P_{ij}^+}}{8\pi}\left(1 - \frac{m_l^2}{m_{P_{ij}^+}}\right)^2 \times (1 + \delta_{\rm em}^{M\ell 2}), \tag{B4}$$

where f_P is the meson decay constant and $\delta_{\rm em}^{M\ell 2}$ is the electromagnetic radiative corrections.

In particular, in order to determine $|V_{us}|$, the ratio among the kaon and pion decay widths into muons is used, which gets a scalar contribution that is dominated by $2\Delta_{us} \approx 2\varsigma_l^* \varsigma_d m_K^2 / M_{H^\pm}$. Since ς_l^* and ς_d can, in general, reach quite high values, we cannot neglect the scalar contribution in this case, and therefore we cannot utilize this for the $|V_{us}|$ determination.

Note that the determination of $|V_{us}|$ obtained from the average of measurements involving leptonic decays ($|V_{us}| = 0.2252 \pm 0.0005$) is not compatible by more than 2 standard deviations with the determination derived from the average of measurements involving semileptonic decays ($|V_{us}| = 0.2231 \pm 0.0006$). When these two determinations are combined in the PDG average, the total uncertainty of the mean value is multiplied by a factor of 2 ($|V_{us}| = 0.2243 \pm 0.0008$) in order to account for the discrepancy among them. In our case, we could attribute the discrepancy to the NP effects. However, using only the determination from semileptonic decays generates a deviation from unitarity in the first row of the CKM matrix above the 3σ level, when combined with $|V_{ud}|$ from nuclear β decays. This "Cabibbo anomaly" is already present in the PDG average, although at a slightly lower level because the leptonic kaon decay pushes the central value of $|V_{us}|$ in a more favorable direction and the uncertainty is increased. In order to relax the deviation from unitarity below the 3σ level, and also motivated by the PDG procedure, we follow a more conservative approach and also increase the uncertainty on $|V_{us}|$ by a factor of 2 (as the PDG does). The final value used in our fits is then

$$|V_{us}| = 0.2230 \pm 0.0012. \tag{B5}$$

c. Determination of $|V_{cd}|$

The PDG [101] average is obtained from semileptonic decays of D mesons to light leptons, leptonic D decays to muons and taus, and neutrino scattering data. The scalar contribution to the leptonic decay can be sizable and therefore we only use the data coming from semileptonic decays ($|V_{cd}| = 0.2330 \pm 0.0136$) and the neutrino scattering data ($|V_{cd}| = 0.230 \pm 0.011$). Averaging these two values, we obtain

$$|V_{cd}| = 0.231 \pm 0.009. \tag{B6}$$

Note, however, that the uncertainty is significantly higher than that of $|V_{us}|$, so the impact of this measurement on the CKM fit is basically negligible.

d. Determination of $|V_{cs}|$

Similar to the previous case, the determination of $|V_{cs}|$ is obtained from measurements of semileptonic decays of D mesons and the leptonic decay of D_s, provided that the form factors are obtained from lattice QCD computations. We dismiss the determination from leptonic decays and we only use the one coming from semileptonic decays:

$$|V_{cs}| = 0.972 \pm 0.007. \tag{B7}$$

As happens for $|V_{cd}|$, we have a much higher uncertainty compared to the light-quark data ($|V_{ud}|$) so, again, this

observable could be neglected from our fit while leaving the results unchanged.

e. Determinations of $|V_{cb}|$ and $|V_{ub}|$

The methods used to determine $|V_{cb}|$ and $|V_{ub}|$ in the PDG do not receive sizable contributions from our additional scalars. Note that, as before, the leptonic decay of the B mesons would be affected by the NP but these processes are not used for the current world average due to their large uncertainty. The values quoted by the PDG [101] are

$$|V_{cb}| = (40.8 \pm 1.4) \times 10^{-3} \tag{B8}$$

and

$$|V_{ub}| = (3.82 \pm 0.20) \times 10^{-3}. \tag{B9}$$

f. Determination of $|V_{td}/V_{ts}|$

Finally, we use the determination of $|V_{td}/V_{ts}|$, which is obtained from measurements of $B^0_{(s)} - \bar{B}^0_{(s)}$ meson mixing. Obviously, the additional scalars will contribute to this mixing but, once the ratio of the B_d and B_s transitions is taken, the NP contribution is highly suppressed since it is only present through SU(3)-breaking effects. We adopt the value for $|V_{td}/V_{ts}|$ quoted by the PDG [101]:

$$|V_{td}/V_{ts}| = (0.207 \pm 0.001 \pm 0.003). \tag{B10}$$

TABLE VIII. Wolfenstein parameters obtained from a fit to the CKM entries in Appendix B 1.

	Value	Correlation			
		λ	A	$\bar{\rho}$	$\bar{\eta}$
λ	0.2249 ± 0.0009	1	−0.22	0.16	−0.13
A	0.806 ± 0.028	−0.22	1	−0.37	−0.49
$\bar{\rho}$	0.173 ± 0.016	0.16	−0.37	1	0.41
$\bar{\eta}$	0.368 ± 0.024	−0.13	−0.49	0.41	1

g. CKM fit result

Using as inputs all of the measurements mentioned in the previous sections, we obtain the values for the Wolfenstein parameters shown in Table VIII.

2. Noncontaminated fit to the oblique parameters

For the determination of the oblique parameters, a global fit of the electroweak observables is performed, removing the contribution from R_b. We use the same inputs as described in Ref. [103], but we remove R_b and use the PDG value for M_W.

TABLE IX. Results for the fit of the oblique parameters S, T, and U, excluding the information from R_b.

	Value	Correlation			Value	Correlation	
		S	T	U		S	T
S	0.005 ± 0.096	1.00	0.91	−0.62	0.024 ± 0.076	1	0.91
T	0.042 ± 0.118	0.91	1.00	−0.84	0.075 ± 0.063	0.91	1
U	0.030 ± 0.091	−0.62	−0.84	1.00			

[1] ATLAS Collaboration, Observation of a new particle in the search for the Standard Model Higgs boson with the ATLAS detector at the LHC, Phys. Lett. B **716**, 1 (2012).

[2] CMS Collaboration, Observation of a new boson at a mass of 125 GeV with the CMS experiment at the LHC, Phys. Lett. B **716**, 30 (2012).

[3] UTfit Collaboration, New UTfit analysis of the unitarity triangle in the Cabibbo-Kobayashi-Maskawa scheme, Rend. Lincei Sci. Fis. Nat. **34**, 37 (2023).

[4] ALEPH, DELPHI, L3, OPAL, SLD, LEP Electroweak Working Group, SLD Electroweak Group, SLD Heavy Flavour Group Collaborations, Precision electroweak measurements on the Z resonance, Phys. Rep. **427**, 257 (2006).

[5] J. L. Diaz-Cruz and D. A. Lopez-Falcon, Probing the mechanism of EWSB with a rho-parameter defined in terms of Higgs couplings, Phys. Lett. B **568**, 245 (2003).

[6] G. C. Branco, P. M. Ferreira, L. Lavoura, M. N. Rebelo, M. Sher, and J. P. Silva, Theory and phenomenology of two-Higgs-doublet models, Phys. Rep. **516**, 1 (2012).

[7] J. F. Gunion, H. E. Haber, G. L. Kane, and S. Dawson, The Higgs Hunter's guide, Front. Phys. **80**, 1 (2000).

[8] I. P. Ivanov, Building and testing models with extended Higgs sectors, Prog. Part. Nucl. Phys. **95**, 160 (2017).

[9] J. F. Gunion and H. E. Haber, Conditions for CP-violation in the general two-Higgs-doublet model, Phys. Rev. D **72**, 095002 (2005).

[10] Y. L. Wu and L. Wolfenstein, Sources of *CP* violation in the two Higgs doublet model, Phys. Rev. Lett. **73**, 1762 (1994).

[11] V. Keus, S. F. King, S. Moretti, and K. Yagyu, *CP* violating two-Higgs-doublet model: Constraints and LHC predictions, J. High Energy Phys. 04 (2016) 048.

[12] C.-Y. Chen, H.-L. Li, and M. Ramsey-Musolf, *CP*-violation in the two Higgs doublet model: From the LHC to EDMs, Phys. Rev. D **97**, 015020 (2018).

[13] S. Iguro and Y. Omura, The direct *CP* violation in a general two Higgs doublet model, J. High Energy Phys. 08 (2019) 098.

[14] J. E. Kim, Light pseudoscalars, particle physics and cosmology, Phys. Rep. **150**, 1 (1987).

[15] D. Espriu, F. Mescia, and A. Renau, Axion-Higgs interplay in the two Higgs-doublet model, Phys. Rev. D **92**, 095013 (2015).

[16] A. Celis, J. Fuentes-Martín, and H. Serôdio, Effective aligned 2HDM with a DFSZ-like invisible axion, Phys. Lett. B **737**, 185 (2014).

[17] L. Lopez Honorez, E. Nezri, J. F. Oliver, and M. H. G. Tytgat, The inert doublet model: An archetype for dark matter, J. Cosmol. Astropart. Phys. 02 (2007) 028.

[18] A. Belyaev, G. Cacciapaglia, I. P. Ivanov, F. Rojas-Abatte, and M. Thomas, Anatomy of the inert two Higgs doublet model in the light of the LHC and non-LHC dark matter searches, Phys. Rev. D **97**, 035011 (2018).

[19] Y.-L. S. Tsai, V. Q. Tran, and C.-T. Lu, Confronting dark matter co-annihilation of inert two Higgs doublet model with a compressed mass spectrum, J. High Energy Phys. 06 (2020) 033.

[20] E. Ma, Verifiable radiative seesaw mechanism of neutrino mass and dark matter, Phys. Rev. D **73**, 077301 (2006).

[21] M. Hirsch, R. A. Lineros, S. Morisi, J. Palacio, N. Rojas, and J. W. F. Valle, WIMP dark matter as radiative neutrino mass messenger, J. High Energy Phys. 10 (2013) 149.

[22] N. Turok and J. Zadrozny, Electroweak baryogenesis in the two doublet model, Nucl. Phys. **B358**, 471 (1991).

[23] J. M. Cline, K. Kainulainen, and M. Trott, Electroweak baryogenesis in two Higgs doublet models and b meson anomalies, J. High Energy Phys. 11 (2011) 089.

[24] K. Fuyuto and E. Senaha, Sphaleron and critical bubble in the scale invariant two Higgs doublet model, Phys. Lett. B **747**, 152 (2015).

[25] P. Ferreira, H. E. Haber, and E. Santos, Preserving the validity of the two-Higgs doublet model up to the Planck scale, Phys. Rev. D **92**, 033003 (2015).

[26] D. Das and I. Saha, Search for a stable alignment limit in two-Higgs-doublet models, Phys. Rev. D **91**, 095024 (2015).

[27] P. Schuh, Vacuum stability of asymptotically safe two Higgs doublet models, Eur. Phys. J. C **79**, 909 (2019).

[28] S. L. Glashow and S. Weinberg, Natural conservation laws for neutral currents, Phys. Rev. D **15**, 1958 (1977).

[29] E. A. Paschos, Diagonal neutral currents, Phys. Rev. D **15**, 1966 (1977).

[30] A. Pich and P. Tuzon, Yukawa alignment in the two-Higgs-doublet model, Phys. Rev. D **80**, 091702 (2009).

[31] A. Pich, Flavour constraints on multi-Higgs-doublet models: Yukawa alignment, Nucl. Phys. B, Proc. Suppl. **209**, 182 (2010).

[32] A. Peñuelas and A. Pich, Flavour alignment in multi-Higgs-doublet models, J. High Energy Phys. 12 (2017) 084.

[33] A. V. Manohar and M. B. Wise, Flavor changing neutral currents, an extended scalar sector, and the Higgs production rate at the CERN LHC, Phys. Rev. D **74**, 035009 (2006).

[34] R. S. Chivukula and H. Georgi, Composite technicolor standard model, Phys. Lett. B **188**, 99 (1987).

[35] G. D'Ambrosio, G. F. Giudice, G. Isidori, and A. Strumia, Minimal flavor violation: An effective field theory approach, Nucl. Phys. **B645**, 155 (2002).

[36] P. M. Ferreira, L. Lavoura, and J. P. Silva, Renormalization-group constraints on Yukawa alignment in multi-Higgs-doublet models, Phys. Lett. B **688**, 341 (2010).

[37] M. Jung, A. Pich, and P. Tuzon, Charged-Higgs phenomenology in the aligned two-Higgs-doublet model, J. High Energy Phys. 11 (2010) 003.

[38] C. B. Braeuninger, A. Ibarra, and C. Simonetto, Radiatively induced flavour violation in the general two-Higgs doublet model with Yukawa alignment, Phys. Lett. B **692**, 189 (2010).

[39] J. Bijnens, J. Lu, and J. Rathsman, Constraining general two Higgs doublet models by the evolution of Yukawa couplings, J. High Energy Phys. 05 (2012) 118.

[40] X.-Q. Li, J. Lu, and A. Pich, $B^0_{s,d} \to \ell^+\ell^-$ decays in the aligned two-Higgs-doublet model, J. High Energy Phys. 06 (2014) 022.

[41] F. J. Botella, G. C. Branco, A. M. Coutinho, M. N. Rebelo, and J. I. Silva-Marcos, Natural quasi-alignment with two Higgs doublets and RGE stability, Eur. Phys. J. C **75**, 286 (2015).

[42] S. Gori, H. E. Haber, and E. Santos, High scale flavor alignment in two-Higgs doublet models and its phenomenology, J. High Energy Phys. 06 (2017) 110.

[43] G. Abbas, A. Celis, X.-Q. Li, J. Lu, and A. Pich, Flavour-changing top decays in the aligned two-Higgs-doublet model, J. High Energy Phys. 06 (2015) 005.

[44] A. Celis, V. Ilisie, and A. Pich, LHC constraints on two-Higgs doublet models, J. High Energy Phys. 07 (2013) 053.

[45] A. Celis, V. Ilisie, and A. Pich, Towards a general analysis of LHC data within two-Higgs-doublet models, J. High Energy Phys. 12 (2013) 095.

[46] M. Jung, A. Pich, and P. Tuzon, The $\bar{B} \to X_s\gamma$ rate and *CP* asymmetry within the aligned two-Higgs-doublet model, Phys. Rev. D **83**, 074011 (2011).

[47] M. Jung, X.-Q. Li, and A. Pich, Exclusive radiative B-meson decays within the aligned two-Higgs-doublet model, J. High Energy Phys. 10 (2012) 063.

[48] V. Ilisie and A. Pich, Low-mass fermiophobic charged Higgs phenomenology in two-Higgs-doublet models, J. High Energy Phys. 09 (2014) 089.

[49] D. Chowdhury and O. Eberhardt, Update of global two-Higgs-doublet model fits, J. High Energy Phys. 05 (2018) 161.

[50] J. Haller, A. Hoecker, R. Kogler, K. Mönig, T. Peiffer, and J. Stelzer, Update of the global electroweak fit and constraints on two-Higgs-doublet models, Eur. Phys. J. C **78**, 675 (2018).

[51] V. Cacchio, D. Chowdhury, O. Eberhardt, and C. W. Murphy, Next-to-leading order unitarity fits in two-Higgs-doublet models with soft $\mathbb{Z}_2$ breaking, J. High Energy Phys. 11 (2016) 026.
[52] D. Chowdhury and O. Eberhardt, Global fits of the two-loop renormalized two-Higgs-doublet model with soft Z_2 breaking, J. High Energy Phys. 11 (2015) 052.
[53] O. Eberhardt, U. Nierste, and M. Wiebusch, Status of the two-Higgs-doublet model of type II, J. High Energy Phys. 07 (2013) 118.
[54] L. Wang and X.-F. Han, Status of the aligned two-Higgs-doublet model confronted with the Higgs data, J. High Energy Phys. 04 (2014) 128.
[55] F. J. Botella, G. C. Branco, M. Nebot, and M. N. Rebelo, Flavour changing Higgs couplings in a class of two Higgs doublet models, Eur. Phys. J. C **76**, 161 (2016).
[56] N. Craig, F. D'Eramo, P. Draper, S. Thomas, and H. Zhang, The hunt for the rest of the Higgs bosons, J. High Energy Phys. 06 (2015) 137.
[57] J. Bernon, J. F. Gunion, Y. Jiang, and S. Kraml, Light Higgs bosons in two-Higgs-doublet models, Phys. Rev. D **91**, 075019 (2015).
[58] J. Bernon, J. F. Gunion, H. E. Haber, Y. Jiang, and S. Kraml, Scrutinizing the alignment limit in two-Higgs-doublet models: $m_h = 125$ GeV, Phys. Rev. D **92**, 075004 (2015).
[59] J. Bernon, J. F. Gunion, H. E. Haber, Y. Jiang, and S. Kraml, Scrutinizing the alignment limit in two-Higgs-doublet models. II. $m_H = 125$ GeV, Phys. Rev. D **93**, 035027 (2016).
[60] A. Ilnicka, M. Krawczyk, and T. Robens, Inert doublet model in light of LHC Run I and astrophysical data, Phys. Rev. D **93**, 055026 (2016).
[61] H. Bélusca-Maïto, A. Falkowski, D. Fontes, J. C. Romão, and J. P. Silva, Higgs EFT for 2HDM and beyond, Eur. Phys. J. C **77**, 176 (2017).
[62] D. Dercks and T. Robens, Constraining the inert doublet model using vector boson fusion, Eur. Phys. J. C **79**, 924 (2019).
[63] A. Ilnicka, T. Robens, and T. Stefaniak, Constraining extended scalar sectors at the LHC and beyond, Mod. Phys. Lett. A **33**, 1830007 (2018).
[64] P. Sanyal, Limits on the charged Higgs parameters in the two Higgs doublet model using CMS $\sqrt{s} = 13$ TeV results, Eur. Phys. J. C **79**, 913 (2019).
[65] J. Herrero-Garcia, M. Nebot, F. Rajec, M. White, and A. G. Williams, Higgs quark flavor violation: Simplified models and status of general two-Higgs-doublet model, J. High Energy Phys. 02 (2020) 147.
[66] S. Karmakar and S. Rakshit, Relaxed constraints on the heavy scalar masses in 2HDM, Phys. Rev. D **100**, 055016 (2019).
[67] N. Chen, T. Han, S. Li, S. Su, W. Su, and Y. Wu, Type-I 2HDM under the Higgs and electroweak precision measurements, J. High Energy Phys. 08 (2020) 131.
[68] F. Arco, S. Heinemeyer, and M. J. Herrero, Exploring sizable triple Higgs couplings in the 2HDM, Eur. Phys. J. C **80**, 884 (2020).
[69] F. J. Botella, F. Cornet-Gomez, and M. Nebot, Flavor conservation in two-Higgs-doublet models, Phys. Rev. D **98**, 035046 (2018).
[70] F. J. Botella, F. Cornet-Gomez, and M. Nebot, Electron and muon $g-2$ anomalies in general flavour conserving two Higgs doublets models, Phys. Rev. D **102**, 035023 (2020).
[71] F. J. Botella, F. Cornet-Gomez, C. Miró, and M. Nebot, Muon and electron $g-2$ anomalies in a flavor conserving 2HDM with an oblique view on the CDF M_W value, Eur. Phys. J. C **82**, 915 (2022).
[72] F. J. Botella, F. Cornet-Gomez, C. Miró, and M. Nebot, New physics hints from τ scalar interactions and $(g-2)_{e,\mu}$, arXiv:2302.05471.
[73] P. Athron, C. Balazs, T. E. Gonzalo, D. Jacob, F. Mahmoudi, and C. Sierra, Likelihood analysis of the flavour anomalies and $g-2$ in the general two Higgs doublet model, J. High Energy Phys. 01 (2022) 037.
[74] O. Eberhardt, A. Peñuelas Martínez, and A. Pich, Global fits in the aligned two-Higgs-doublet model, J. High Energy Phys. 05 (2021) 005.
[75] J. M. Connell, P. M. Ferreira, and H. E. Haber, Accommodating hints of new heavy scalars in the framework of the flavor-aligned two-Higgs-doublet model, Phys. Rev. D **108**, 055031 (2023).
[76] A. Karan, V. Miralles, and A. Pich, Global fit of the Aligned Two-Higgs-Doublet Model, arXiv:2312.00514.
[77] J. De Blas *et al.*, HEPfit: A code for the combination of indirect and direct constraints on high energy physics models, Eur. Phys. J. C **80**, 456 (2020).
[78] CDF Collaboration, High-precision measurement of the W boson mass with the CDF II detector, Science **376**, 170 (2022).
[79] T. Aoyama *et al.*, The anomalous magnetic moment of the muon in the standard model, Phys. Rep. **887**, 1 (2020).
[80] S. Borsanyi *et al.*, Leading hadronic contribution to the muon magnetic moment from lattice QCD, Nature (London) **593**, 51 (2021).
[81] M. Cè *et al.*, Window observable for the hadronic vacuum polarization contribution to the muon $g-2$ from lattice QCD, Phys. Rev. D **106**, 114502 (2022).
[82] Extended Twisted Mass Collaboration, Lattice calculation of the short and intermediate time-distance hadronic vacuum polarization contributions to the muon magnetic moment using twisted-mass fermions, Phys. Rev. D **107**, 074506 (2023).
[83] M. Davier, A. Hoecker, G. Lopez Castro, B. Malaescu, X. H. Mo, G. Toledo Sanchez, P. Wang, C. Z. Yuan, and Z. Zhang, The discrepancy between τ and e^+e^- spectral functions revisited and the consequences for the muon magnetic anomaly, Eur. Phys. J. C **66**, 127 (2010).
[84] A. Pich, Precision tau physics, Prog. Part. Nucl. Phys. **75**, 41 (2014).
[85] J. de Blas, M. Ciuchini, E. Franco, A. Goncalves, S. Mishima, M. Pierini, L. Reina, and L. Silvestrini, Global analysis of electroweak data in the Standard Model, Phys. Rev. D **106**, 033003 (2022).
[86] G. Durieux, A. Irles, V. Miralles, A. Peñuelas, R. Pöschl, M. Perelló, R. Pöschl, and M. Vos, The electro-weak couplings of the top and bottom quarks—Global fit and future prospects, J. High Energy Phys. 12 (2019) 098.
[87] V. Miralles, M. M. López, M. M. Llácer, A. Peñuelas, M. Perelló, and M. Vos, The top quark electro-weak couplings after LHC Run 2, J. High Energy Phys. 02 (2022) 032.

[88] O. Eberhardt, V. Miralles, and A. Pich, Constraints on coloured scalars from global fits, J. High Energy Phys. 10 (2021) 123.

[89] I. P. Ivanov, Minkowski space structure of the Higgs potential in 2HDM, Phys. Rev. D **75**, 035001 (2007).

[90] I. P. Ivanov and J. P. Silva, Tree-level metastability bounds for the most general two Higgs doublet model, Phys. Rev. D **92**, 055017 (2015).

[91] H. Bahl, M. Carena, N. M. Coyle, A. Ireland, and C. E. M. Wagner, New tools for dissecting the general 2HDM, J. High Energy Phys. 03 (2023) 165.

[92] P. M. Ferreira, R. Santos, and A. Barroso, Stability of the tree-level vacuum in two Higgs doublet models against charge or *CP* spontaneous violation, Phys. Lett. B **603**, 219 (2004).

[93] A. Barroso, P. M. Ferreira, I. P. Ivanov, and R. Santos, Metastability bounds on the two Higgs doublet model, J. High Energy Phys. 06 (2013) 045.

[94] I. F. Ginzburg and I. P. Ivanov, Tree-level unitarity constraints in the most general 2HDM, Phys. Rev. D **72**, 115010 (2005).

[95] L. Allwicher, P. Arnan, D. Barducci, and M. Nardecchia, Perturbative unitarity constraints on generic Yukawa interactions, J. High Energy Phys. 10 (2021) 129.

[96] M. E. Peskin and T. Takeuchi, A new constraint on a strongly interacting Higgs sector, Phys. Rev. Lett. **65**, 964 (1990).

[97] M. E. Peskin and T. Takeuchi, Estimation of oblique electroweak corrections, Phys. Rev. D **46**, 381 (1992).

[98] H. E. Haber and D. O'Neil, Basis-independent methods for the two-Higgs-doublet model III: The *CP*-conserving limit, custodial symmetry, and the oblique parameters S, T, U, Phys. Rev. D **83**, 055017 (2011).

[99] H. E. Haber and H. E. Logan, Radiative corrections to the $Zb\bar{b}$ vertex and constraints on extended Higgs sectors, Phys. Rev. D **62**, 015011 (2000).

[100] G. Degrassi and P. Slavich, QCD corrections in two-Higgs-doublet extensions of the standard model with minimal flavor violation, Phys. Rev. D **81**, 075001 (2010).

[101] Particle Data Group, Review of particle physics, Prog. Theor. Exp. Phys. **2022**, 083C01 (2022).

[102] J. de Blas, M. Ciuchini, E. Franco, S. Mishima, M. Pierini, L. Reina, and L. Silvestrini, Electroweak precision observables and Higgs-boson signal strengths in the Standard Model and beyond: Present and future, J. High Energy Phys. 12 (2016) 135.

[103] J. de Blas, M. Pierini, L. Reina, and L. Silvestrini, Impact of the recent measurements of the top-quark and W-boson masses on electroweak precision fits, Phys. Rev. Lett. **129**, 271801 (2022).

[104] L. Wolfenstein, Parametrization of the Kobayashi-Maskawa matrix, Phys. Rev. Lett. **51**, 1945 (1983).

[105] CKMfitter Group, *CP* violation and the CKM matrix: Assessing the impact of the asymmetric *B* factories, Eur. Phys. J. C **41**, 1 (2005).

[106] UTfit Collaboration, The unitarity triangle fit in the standard model and hadronic parameters from lattice QCD: A reappraisal after the measurements of Δm_s and $BR(B \to \tau\nu_\tau)$, J. High Energy Phys. 10 (2006) 081.

[107] UTfit Collaboration, The UTfit Collaboration report on the status of the unitarity triangle beyond the standard model. I. Model-independent analysis and minimal flavor violation, J. High Energy Phys. 03 (2006) 080.

[108] Q. Chang, P.-F. Li, and X.-Q. Li, B_s^0–$\bar{B}_s^0$ mixing within minimal flavor-violating two-Higgs-doublet models, Eur. Phys. J. C **75**, 594 (2015).

[109] C. Bobeth, M. Misiak, and J. Urban, Matching conditions for $b \to s\gamma$ and $b \to sgluon$ in extensions of the standard model, Nucl. Phys. **B567**, 153 (2000).

[110] M. Misiak and M. Steinhauser, NNLO QCD corrections to the $\bar{B} \to X_s\gamma$ matrix elements using interpolation in m_c, Nucl. Phys. **B764**, 62 (2007).

[111] M. Misiak *et al.*, Estimate of $\mathcal{B}(\bar{B} \to X_s\gamma)$ at $O(\alpha_s^2)$, Phys. Rev. Lett. **98**, 022002 (2007).

[112] T. Hermann, M. Misiak, and M. Steinhauser, $\bar{B} \to X_s\gamma$ in the two Higgs doublet model up to next-to-next-to-leading order in QCD, J. High Energy Phys. 11 (2012) 036.

[113] M. Misiak *et al.*, Updated NNLO QCD predictions for the weak radiative B-meson decays, Phys. Rev. Lett. **114**, 221801 (2015).

[114] M. Misiak, A. Rehman, and M. Steinhauser, NNLO QCD counterterm contributions to $\bar{B} \to X_{s\gamma}$ for the physical value of m_c, Phys. Lett. B **770**, 431 (2017).

[115] M. Misiak, A. Rehman, and M. Steinhauser, Towards $\bar{B} \to X_s\gamma$ at the NNLO in QCD without interpolation in m_c, J. High Energy Phys. 06 (2020) 175.

[116] P. Arnan, D. Bečirević, F. Mescia, and O. Sumensari, Two Higgs doublet models and $b \to s$ exclusive decays, Eur. Phys. J. C **77**, 796 (2017).

[117] V. Ilisie, New Barr-Zee contributions to $(\mathbf{g-2})_\mu$ in two-Higgs-doublet models, J. High Energy Phys. 04 (2015) 077.

[118] Muon $g-2$ Collaboration, Measurement of the positive muon anomalous magnetic moment to 0.46 ppm, Phys. Rev. Lett. **126**, 141801 (2021).

[119] Muon $g-2$ Collaboration, Measurement of the positive muon anomalous magnetic moment to 0.20 ppm, Phys. Rev. Lett. **131**, 161802 (2023).

[120] M. Davier, D. Díaz-Calderón, B. Malaescu, A. Pich, A. Rodríguez-Sánchez, and Z. Zhang, The Euclidean Adler function and its interplay with $\Delta\alpha_{\mathrm{QED}}^{\mathrm{had}}$ and α_s, J. High Energy Phys. 04 (2023) 067.

[121] CMD-3 Collaboration, Measurement of the $e^+e^- \to \pi^+\pi^-$ cross section from threshold to 1.2 GeV with the CMD-3 detector, arXiv:2302.08834.

[122] ATLAS Collaboration, Measurement of the *W*-boson mass in pp collisions at $\sqrt{s} = 7$ TeV with the ATLAS detector, Eur. Phys. J. C **78**, 110 (2018).

[123] ATLAS Collaboration, Improved W boson mass measurement using 7 TeV proton-proton collisions with the ATLAS detector, Report No. ATLAS-CONF-2023-004, 2023.

[124] ATLAS Collaboration, Direct constraint on the Higgs-charm coupling from a search for Higgs boson decays to charm quarks with the ATLAS detector, Report No. ATLAS-CONF-2021-021, 2021.

[125] CMS Collaboration, A search for the standard model Higgs boson decaying to charm quarks, J. High Energy Phys. 03 (2020) 131.

[126] ATLAS Collaboration, Search for the $b\bar{b}$ decay of the Standard Model Higgs boson in associated $(W/Z)H$

production with the ATLAS detector, J. High Energy Phys. 01 (2015) 069.
[127] ATLAS Collaboration, Search for the standard model Higgs boson produced in association with top quarks and decaying into $b\bar{b}$ in pp collisions at $\sqrt{s} = 8$ TeV with the ATLAS detector, Eur. Phys. J. C **75**, 349 (2015).
[128] CMS Collaboration, Search for the standard model Higgs boson produced in association with a W or a Z boson and decaying to bottom quarks, Phys. Rev. D **89**, 012003 (2014).
[129] CMS Collaboration, Search for the associated production of the Higgs boson with a top-quark pair, J. High Energy Phys. 09 (2014) 087.
[130] ATLAS Collaboration, Measurements of Higgs bosons decaying to bottom quarks from vector boson fusion production with the ATLAS experiment at $\sqrt{s} = 13$ TeV, Eur. Phys. J. C **81**, 537 (2021).
[131] ATLAS Collaboration, Measurements of WH and ZH production in the $H \to b\bar{b}$ decay channel in pp collisions at 13 TeV with the ATLAS detector, Eur. Phys. J. C **81**, 178 (2021).
[132] CMS Collaboration, VBF H to bb using the 2015 data sample, Report No. CMS-PAS-HIG-16-003, 2016.
[133] CMS Collaboration, Observation of Higgs boson decay to bottom quarks, Phys. Rev. Lett. **121**, 121801 (2018).
[134] ATLAS Collaboration, Measurement of Higgs boson production in the diphoton decay channel in pp collisions at center-of-mass energies of 7 and 8 TeV with the ATLAS detector, Phys. Rev. D **90**, 112015 (2014).
[135] CMS Collaboration, Observation of the diphoton decay of the Higgs boson and measurement of its properties, Eur. Phys. J. C **74**, 3076 (2014).
[136] ATLAS Collaboration, Measurement of the properties of Higgs boson production at $\sqrt{s} = 13$ TeV in the $H \to \gamma\gamma$ channel using 139 fb^{-1} of pp collision data with the ATLAS experiment, Report No. ATLAS-CONF-2020-026, 2020.
[137] CMS Collaboration, Measurements of Higgs boson production cross sections and couplings in the diphoton decay channel at $\sqrt{s} = 13$ TeV, J. High Energy Phys. 07 (2021) 027.
[138] ATLAS, CMS Collaborations, Measurements of the Higgs boson production and decay rates and constraints on its couplings from a combined ATLAS and CMS analysis of the LHC pp collision data at $\sqrt{s} = 7$ and 8 TeV, J. High Energy Phys. 08 (2016) 045.
[139] ATLAS Collaboration, A search for the dimuon decay of the Standard Model Higgs boson with the ATLAS detector, Phys. Lett. B **812**, 135980 (2021).
[140] CMS Collaboration, Evidence for Higgs boson decay to a pair of muons, J. High Energy Phys. 01 (2021) 148.
[141] ATLAS Collaboration, Evidence for the Higgs-boson Yukawa coupling to tau leptons with the ATLAS detector, J. High Energy Phys. 04 (2015) 117.
[142] CMS Collaboration, Evidence for the 125 GeV Higgs boson decaying to a pair of τ leptons, J. High Energy Phys. 05 (2014) 104.
[143] ATLAS Collaboration, A combination of measurements of Higgs boson production and decay using up to 139 fb^{-1} of proton–proton collision data at $\sqrt{s} = 13$ TeV collected with the ATLAS experiment, Report No. ATLAS-CONF-2020-027, 2020.
[144] CMS Collaboration, Combined Higgs boson production and decay measurements with up to 137 fb^{-1} of proton-proton collision data at $\sqrt{s} = 13$ TeV, Report No. CMS-PAS-HIG-19-005, 2020.
[145] ATLAS Collaboration, Observation and measurement of Higgs boson decays to WW* with the ATLAS detector, Phys. Rev. D **92**, 012006 (2015).
[146] ATLAS Collaboration, Study of (W/Z)H production and Higgs boson couplings using $H \to WW^*$ decays with the ATLAS detector, J. High Energy Phys. 08 (2015) 137.
[147] CMS Collaboration, Measurement of Higgs boson production and properties in the WW decay channel with leptonic final states, J. High Energy Phys. 01 (2014) 096.
[148] ATLAS Collaboration, Measurements of the Higgs boson production and decay rates and coupling strengths using pp collision data at $\sqrt{s} = 7$ and 8 TeV in the ATLAS experiment, Eur. Phys. J. C **76**, 6 (2016).
[149] CMS Collaboration, Search for a Higgs boson decaying into a Z and a photon in pp collisions at $\sqrt{s} = 7$ and 8 TeV, Phys. Lett. B **726**, 587 (2013).
[150] ATLAS Collaboration, A search for the $Z\gamma$ decay mode of the Higgs boson in pp collisions at $\sqrt{s} = 13$ TeV with the ATLAS detector, Phys. Lett. B **809**, 135754 (2020).
[151] CMS Collaboration, Search for the decay of a Higgs boson in the $\ell\ell\gamma$ channel in proton-proton collisions at $\sqrt{s} = 13$ TeV, J. High Energy Phys. 11 (2018) 152.
[152] ATLAS Collaboration, Measurements of Higgs boson production and couplings in the four-lepton channel in pp collisions at center-of-mass energies of 7 and 8 TeV with the ATLAS detector, Phys. Rev. D **91**, 012006 (2015).
[153] CMS Collaboration, Precise determination of the mass of the Higgs boson and tests of compatibility of its couplings with the standard model predictions using proton collisions at 7 and 8 TeV, Eur. Phys. J. C **75**, 212 (2015).
[154] ATLAS Collaboration, Higgs boson production cross-section measurements and their EFT interpretation in the 4ℓ decay channel at $\sqrt{s} = 13$ TeV with the ATLAS detector, Eur. Phys. J. C **80**, 957 (2020).
[155] ATLAS Collaboration, Search for charged Higgs bosons decaying via $H^\pm \to \tau^\pm\nu$ in fully hadronic final states using pp collision data at $\sqrt{s} = 8$ TeV with the ATLAS detector, J. High Energy Phys. 03 (2015) 088.
[156] CMS Collaboration, Search for a charged Higgs boson in pp collisions at $\sqrt{s} = 8$ TeV, J. High Energy Phys. 11 (2015) 018.
[157] ATLAS Collaboration, Search for charged Higgs bosons decaying via $H^\pm \to \tau^\pm\nu_\tau$ in the $\tau +$ jets and $\tau +$ lepton final states with 36 fb^{-1} of pp collision data recorded at $\sqrt{s} = 13$ TeV with the ATLAS experiment, J. High Energy Phys. 09 (2018) 139.
[158] CMS Collaboration, Search for charged Higgs bosons in the $H^\pm \to \tau^\pm\nu_\tau$ decay channel in proton-proton collisions at $\sqrt{s} = 13$ TeV, J. High Energy Phys. 07 (2019) 142.
[159] ATLAS Collaboration, Search for charged Higgs bosons in the $H^\pm \to tb$ decay channel in pp collisions at $\sqrt{s} =$ 8 TeV using the ATLAS detector, J. High Energy Phys. 03 (2016) 127.

[160] ATLAS Collaboration, Search for charged Higgs bosons decaying into a top quark and a bottom quark at $\sqrt{s} =$ 13 TeV with the ATLAS detector, J. High Energy Phys. 06 (2021) 145.
[161] CMS Collaboration, Search for charged Higgs bosons decaying into a top and a bottom quark in the all-jet final state of pp collisions at $\sqrt{s} = 13$ TeV, J. High Energy Phys. 07 (2020) 126.
[162] ATLAS Collaboration, Searches for Higgs boson pair production in the $hh \to bb\tau\tau, \gamma\gamma WW^*, \gamma\gamma bb, bbbb$ channels with the ATLAS detector, Phys. Rev. D **92**, 092004 (2015).
[163] CMS Collaboration, Search for resonant pair production of Higgs bosons decaying to two bottom quark–antiquark pairs in proton–proton collisions at 8 TeV, Phys. Lett. B **749**, 560 (2015).
[164] CMS Collaboration, Search for two Higgs bosons in final states containing two photons and two bottom quarks in proton-proton collisions at 8 TeV, Phys. Rev. D **94**, 052012 (2016).
[165] CMS Collaboration, Searches for a heavy scalar boson H decaying to a pair of 125 GeV Higgs bosons hh or for a heavy pseudoscalar boson A decaying to Zh, in the final states with $h \to \tau\tau$, Phys. Lett. B **755**, 217 (2016).
[166] CMS Collaboration, Search for Higgs boson pair production in the $bb\tau\tau$ final state in proton-proton collisions at $\sqrt{(s)} = 8$ TeV, Phys. Rev. D **96**, 072004 (2017).
[167] ATLAS Collaboration, Search for resonant pair production of Higgs bosons in the $b\bar{b}b\bar{b}$ final state using pp collisions at $\sqrt{s} = 13$ TeV with the ATLAS detector, Phys. Rev. D **105**, 092002 (2022).
[168] CMS Collaboration, Search for resonant pair production of Higgs bosons decaying to bottom quark-antiquark pairs in proton-proton collisions at 13 TeV, J. High Energy Phys. 08 (2018) 152.
[169] CMS Collaboration, Search for resonant Higgs boson pair production in four b quark final state using large-area jets in proton-proton collisions at $\sqrt{s} = 13$ TeV, Report No. CMS-PAS-B2G-20-004, 2021.
[170] CMS Collaboration, Search for Higgs boson pairs decaying to WWWW, WW$\tau\tau$, and $\tau\tau\tau\tau$ in proton-proton collisions at $\sqrt{s} = 13$ TeV, J. High Energy Phys. 07 (2023) 095.
[171] ATLAS Collaboration, Search for Higgs boson pair production in the two bottom quarks plus two photons final state in pp collisions at $\sqrt{s} = 13$ TeV with the ATLAS detector, Phys. Rev. D **106**, 052001 (2022).
[172] CMS Collaboration, Search for Higgs boson pair production in the $\gamma\gamma b\bar{b}$ final state in pp collisions at $\sqrt{s} = 13$ TeV, Phys. Lett. B **788**, 7 (2019).
[173] ATLAS Collaboration, Search for resonant and non-resonant Higgs boson pair production in the $b\bar{b}\tau^+\tau^-$ decay channel using 13 TeV pp collision data from the ATLAS detector, Report No. ATLAS-CONF-2021-030, 2021.
[174] ATLAS Collaboration, Reconstruction and identification of boosted di-τ systems in a search for Higgs boson pairs using 13 TeV proton-proton collision data in ATLAS, J. High Energy Phys. 11 (2020) 163.
[175] CMS Collaboration, Search for Higgs boson pair production in events with two bottom quarks and two tau leptons in proton–proton collisions at $\sqrt{s} = 13$ TeV, Phys. Lett. B **778**, 101 (2018).
[176] CMS Collaboration, Search for heavy resonances decaying into two Higgs bosons or into a Higgs boson and a W or Z boson in proton-proton collisions at 13 TeV, J. High Energy Phys. 01 (2019) 051.
[177] CMS Collaboration, Search for resonant and nonresonant Higgs boson pair production in the $b\bar{b}\ell\nu\ell\nu$ final state in proton-proton collisions at $\sqrt{s} = 13$ TeV, J. High Energy Phys. 01 (2018) 054.
[178] CMS Collaboration, Search for resonances decaying to a pair of Higgs bosons in the $b\bar{b}q\bar{q}'\ell\nu$ final state in proton-proton collisions at $\sqrt{s} = 13$ TeV, J. High Energy Phys. 10 (2019) 125.
[179] CMS Collaboration, Search for resonant pair production of Higgs bosons in the $bbZZ$ channel in proton-proton collisions at $\sqrt{s} = 13$ TeV, Phys. Rev. D **102**, 032003 (2020).
[180] ATLAS Collaboration, Search for Higgs boson pair production in the $b\bar{b}WW^*$ decay mode at $\sqrt{s} = 13$ TeV with the ATLAS detector, J. High Energy Phys. 04 (2019) 092.
[181] CMS Collaboration, Search for heavy resonances decaying to a pair of Lorentz-boosted Higgs bosons in final states with leptons and a bottom quark pair at $\sqrt{s} = 13$ TeV, J. High Energy Phys. 05 (2022) 005.
[182] ATLAS Collaboration, Search for Higgs boson pair production in the $\gamma\gamma WW^*$ channel using pp collision data recorded at $\sqrt{s} = 13$ TeV with the ATLAS detector, Eur. Phys. J. C **78**, 1007 (2018).
[183] ATLAS Collaboration, Search for a CP-odd Higgs boson decaying to Zh in pp collisions at $\sqrt{s} = 8$ TeV with the ATLAS detector, Phys. Lett. B **744**, 163 (2015).
[184] CMS Collaboration, Search for a pseudoscalar boson decaying into a Z boson and the 125 GeV Higgs boson in $\ell^+\ell^- b\bar{b}$ final states, Phys. Lett. B **748**, 221 (2015).
[185] ATLAS Collaboration, Search for heavy resonances decaying into a W or Z boson and a Higgs boson in final states with leptons and b-jets in 36 fb^{-1} of $\sqrt{s} = 13$ TeV pp collisions with the ATLAS detector, J. High Energy Phys. 03 (2018) 174.
[186] CMS Collaboration, Search for a heavy pseudoscalar boson decaying to a Z and a Higgs boson at $\sqrt{s} = 13$ TeV, Eur. Phys. J. C **79**, 564 (2019).
[187] CMS Collaboration, Search for heavy resonances decaying into a vector boson and a Higgs boson in final states with charged leptons, neutrinos and b quarks at $\sqrt{s} = 13$ TeV, J. High Energy Phys. 11 (2018) 172.
[188] CMS Collaboration, Search for a heavy pseudoscalar Higgs boson decaying into a 125 GeV Higgs boson and a Z boson in final states with two tau and two light leptons at $\sqrt{s} = 13$ TeV, J. High Energy Phys. 03 (2020) 065.
[189] CMS Collaboration, Search for neutral resonances decaying into a Z boson and a pair of b jets or τ leptons, Phys. Lett. B **759**, 369 (2016).
[190] ATLAS Collaboration, Search for a heavy Higgs boson decaying into a Z boson and another heavy Higgs boson in the $\ell\ell bb$ and $\ell\ell WW$ final states in pp collisions at $\sqrt{s} =$ 13 TeV with the ATLAS detector, Eur. Phys. J. C **81**, 396 (2021).
[191] ATLAS Collaboration, Search for new phenomena in $t\bar{t}$ final states with additional heavy-flavour jets in pp

collisions at $\sqrt{s} = 13$ TeV with the ATLAS detector, Report No. ATLAS-CONF-2016-104, 2016.
[192] CMS Collaboration, Search for production of four top quarks in final states with same-sign or multiple leptons in proton-proton collisions at $\sqrt{s} = 13$ TeV, Eur. Phys. J. C **80**, 75 (2020).
[193] ATLAS Collaboration, Search for $t\bar{t}H/A \to t\bar{t}t\bar{t}$ production in the multilepton final state in proton-proton collisions at $\sqrt{s} = 13$ TeV with the ATLAS detector, Report No. ATLAS-CONF-2022-008, 2022.
[194] CMS Collaboration, Search for neutral MSSM Higgs bosons decaying into a pair of bottom quarks, J. High Energy Phys. 11 (2015) 071.
[195] CMS Collaboration, Search for narrow resonances in the b-tagged dijet mass spectrum in proton-proton collisions at $\sqrt{s} = 8$ TeV, Phys. Rev. Lett. **120**, 201801 (2018).
[196] CMS Collaboration, Search for a narrow heavy decaying to bottom quark pairs in the 13 TeV data sample, Report No. CMS-PAS-HIG-16-025, 2016.
[197] CMS Collaboration, Search for beyond the standard model Higgs bosons decaying into a $b\bar{b}$ pair in pp collisions at $\sqrt{s} = 13$ TeV, J. High Energy Phys. 08 (2018) 113.
[198] ATLAS Collaboration, Search for resonances in the mass distribution of jet pairs with one or two jets identified as b-jets in proton-proton collisions at $\sqrt{s} = 13$ TeV with the ATLAS detector, Phys. Rev. D **98**, 032016 (2018).
[199] ATLAS Collaboration, Search for heavy neutral Higgs bosons produced in association with b-quarks and decaying into b-quarks at $\sqrt{s} = 13$ TeV with the ATLAS detector, Phys. Rev. D **102**, 032004 (2020).
[200] CMS Collaboration, Search for low-mass resonances decaying into bottom quark-antiquark pairs in proton-proton collisions at $\sqrt{s} = 13$ TeV, Phys. Rev. D **99**, 012005 (2019).
[201] CMS Collaboration, Search for neutral MSSM Higgs bosons decaying to $\mu^+\mu^-$ in pp collisions at $\sqrt{s} = 7$ and 8 TeV, Phys. Lett. B **752**, 221 (2016).
[202] CMS Collaboration, Search for MSSM Higgs bosons decaying to $\mu + \mu-$ in proton-proton collisions at s = 13 TeV, Phys. Lett. B **798**, 134992 (2019).
[203] ATLAS Collaboration, Search for scalar resonances decaying into $\mu^+\mu^-$ in events with and without b-tagged jets produced in proton-proton collisions at $\sqrt{s} = 13$ TeV with the ATLAS detector, J. High Energy Phys. 07 (2019) 117.
[204] ATLAS Collaboration, Search for neutral Higgs bosons of the minimal supersymmetric standard model in pp collisions at $\sqrt{s} = 8$ TeV with the ATLAS detector, J. High Energy Phys. 11 (2014) 056.
[205] CMS Collaboration, Search for additional neutral Higgs bosons decaying to a pair of tau leptons in pp collisions at $\sqrt{s} = 7$ and 8 TeV, Report No. CMS-PAS-HIG-14-029, 2015.
[206] ATLAS Collaboration, Search for minimal supersymmetric standard model Higgs bosons H/A and for a Z' boson in the $\tau\tau$ final state produced in pp collisions at $\sqrt{s} =$ 13 TeV with the ATLAS Detector, Eur. Phys. J. C **76**, 585 (2016).
[207] ATLAS Collaboration, Search for heavy Higgs bosons decaying into two tau leptons with the ATLAS detector using pp collisions at $\sqrt{s} = 13$ TeV, Phys. Rev. Lett. **125**, 051801 (2020).
[208] CMS Collaboration, Searches for additional Higgs bosons and vector leptoquarks in $\tau\tau$ final states in proton-proton collisions at $\sqrt{s} = 13$ TeV, Report No. CMS-PAS-HIG-21-001, 2022.
[209] ATLAS Collaboration, Search for additional heavy neutral Higgs and gauge bosons in the ditau final state produced in 36 fb^{-1} of pp collisions at $\sqrt{s} = 13$ TeV with the ATLAS detector, J. High Energy Phys. 01 (2018) 055.
[210] CMS Collaboration, Search for additional neutral MSSM Higgs bosons in the $\tau\tau$ final state in proton-proton collisions at $\sqrt{s} = 13$ TeV, J. High Energy Phys. 09 (2018) 007.
[211] ATLAS Collaboration, Search for scalar diphoton resonances in the mass range 65–600 GeV with the ATLAS detector in pp collision data at $\sqrt{s} = 8$ TeV, Phys. Rev. Lett. **113**, 171801 (2014).
[212] CMS Collaboration, Search for high-mass diphoton resonances in proton–proton collisions at 13 TeV and combination with 8 TeV search, Phys. Lett. B **767**, 147 (2017).
[213] CMS Collaboration, Search for physics beyond the standard model in high-mass diphoton events from proton-proton collisions at $\sqrt{s} = 13$ TeV, Phys. Rev. D **98**, 092001 (2018).
[214] ATLAS Collaboration, Search for resonances decaying into photon pairs in 139 fb^{-1} of pp collisions at $\sqrt{s} =$ 13 TeV with the ATLAS detector, Phys. Lett. B **822**, 136651 (2021).
[215] ATLAS Collaboration, Search for new resonances in $W\gamma$ and $Z\gamma$ final states in pp collisions at $\sqrt{s} = 8$ TeV with the ATLAS detector, Phys. Lett. B **738**, 428 (2014).
[216] CMS Collaboration, Search for scalar resonances in the 200–1200 GeV mass range decaying into a Z and a photon in pp collisions at $\sqrt{s} = 8$ TeV, Report No. CMS-PAS-HIG-16-014, 2016.
[217] CMS Collaboration, Search for $Z\gamma$ resonances using leptonic and hadronic final states in proton-proton collisions at $\sqrt{s} = 13$ TeV, J. High Energy Phys. 09 (2018) 148.
[218] ATLAS Collaboration, Searches for the $Z\gamma$ decay mode of the Higgs boson and for new high-mass resonances in pp collisions at $\sqrt{s} = 13$ TeV with the ATLAS detector, J. High Energy Phys. 10 (2017) 112.
[219] ATLAS Collaboration, Search for heavy resonances decaying to a photon and a hadronically decaying $Z/W/H$ boson in pp collisions at $\sqrt{s} = 13$ TeV with the ATLAS detector, Phys. Rev. D **98**, 032015 (2018).
[220] ATLAS Collaboration, Search for an additional, heavy Higgs boson in the $H \to ZZ$ decay channel at $\sqrt{s} = 8$ TeV in pp collision data with the ATLAS detector, Eur. Phys. J. C **76**, 45 (2016).
[221] ATLAS Collaboration, Search for heavy ZZ resonances in the $\ell^+\ell^-\ell^+\ell^-$ and $\ell^+\ell^-\nu\bar{\nu}$ final states using proton–proton collisions at $\sqrt{s} = 13$ TeV with the ATLAS detector, Eur. Phys. J. C **78**, 293 (2018).
[222] ATLAS Collaboration, Search for heavy resonances decaying into a pair of Z bosons in the $\ell^+\ell^-\ell'^+\ell'^-$ and $\ell^+\ell^-\nu\bar{\nu}$ final states using 139 fb^{-1} of proton–proton collisions at $\sqrt{s} = 13$ TeV with the ATLAS detector, Eur. Phys. J. C **81**, 332 (2021).

[223] ATLAS Collaboration, Searches for heavy ZZ and ZW resonances in the $\ell\ell qq$ and $\nu\nu qq$ final states in pp collisions at $\sqrt{s} = 13$ TeV with the ATLAS detector, J. High Energy Phys. 03 (2018) 009.
[224] CMS Collaboration, Search for a new scalar resonance decaying to a pair of Z bosons in proton-proton collisions at $\sqrt{s} = 13$ TeV, J. High Energy Phys. 06 (2018) 127.
[225] CMS Collaboration, Search for a heavy resonance decaying into a Z boson and a vector boson in the $\nu\bar{\nu}q\bar{q}$ final state, J. High Energy Phys. 07 (2018) 075.
[226] ATLAS Collaboration, Search for a high-mass Higgs boson decaying to a W boson pair in pp collisions at $\sqrt{s} =$ 8 TeV with the ATLAS detector, J. High Energy Phys. 01 (2016) 032.
[227] CMS Collaboration, Search for a heavy Higgs boson decaying to a pair of W bosons in proton-proton collisions at $\sqrt{s} = 13$ TeV, J. High Energy Phys. 03 (2020) 034.
[228] ATLAS Collaboration, Search for heavy resonances decaying into WW in the $e\nu\mu\nu$ final state in pp collisions at $\sqrt{s} = 13$ TeV with the ATLAS detector, Eur. Phys. J. C **78**, 24 (2018).
[229] CMS Collaboration, Search for high mass Higgs to WW with fully leptonic decays using 2015 data, Report No. CMS-PAS-HIG-16-023, 2016.
[230] ATLAS Collaboration, Search for WW/WZ resonance production in $\ell\nu qq$ final states in pp collisions at $\sqrt{s} =$ 13 TeV with the ATLAS detector, J. High Energy Phys. 03 (2018) 042.
[231] CMS Collaboration, Search for a heavy resonance decaying to a pair of vector bosons in the lepton plus merged jet final state at $\sqrt{s} = 13$ TeV, J. High Energy Phys. 05 (2018) 088.
[232] CMS Collaboration, Search for a Higgs boson in the mass range from 145 to 1000 GeV decaying to a pair of W or Z bosons, J. High Energy Phys. 10 (2015) 144.
[233] ATLAS Collaboration, Search for diboson resonances with boson-tagged jets in pp collisions at $\sqrt{s} = 13$ TeV with the ATLAS detector, Phys. Lett. B **777**, 91 (2018).
[234] ATLAS Collaboration, Combination of searches for heavy resonances decaying into bosonic and leptonic final states using 36 fb^{-1} of proton-proton collision data at $\sqrt{s} =$ 13 TeV with the ATLAS detector, Phys. Rev. D **98**, 052008 (2018).
[235] ATLAS Collaboration, Search for heavy diboson resonances in semileptonic final states in pp collisions at $\sqrt{s} =$ 13 TeV with the ATLAS detector, Eur. Phys. J. C **80**, 1165 (2020).
[236] CMS Collaboration, Search for heavy resonances decaying to WW, WZ, or WH boson pairs in the lepton plus merged jet final state in proton-proton collisions at $\sqrt{s} = 13$ TeV, Phys. Rev. D **105**, 032008 (2022).
[237] J. C. Hardy and I. S. Towner, Superallowed $0^+ \to 0^+$ nuclear β decays: 2020 critical survey, with implications for V_{ud} and CKM unitarity, Phys. Rev. C **102**, 045501 (2020).
[238] C.-Y. Seng, D. Galviz, W. J. Marciano, and U.-G. Meißner, Update on $|Vus|$ and $|Vus/Vud|$ from semileptonic kaon and pion decays, Phys. Rev. D **105**, 013005 (2022).
[239] Flavour Lattice Averaging Group (FLAG) Collaboration, FLAG review 2021, Eur. Phys. J. C **82**, 869 (2022).